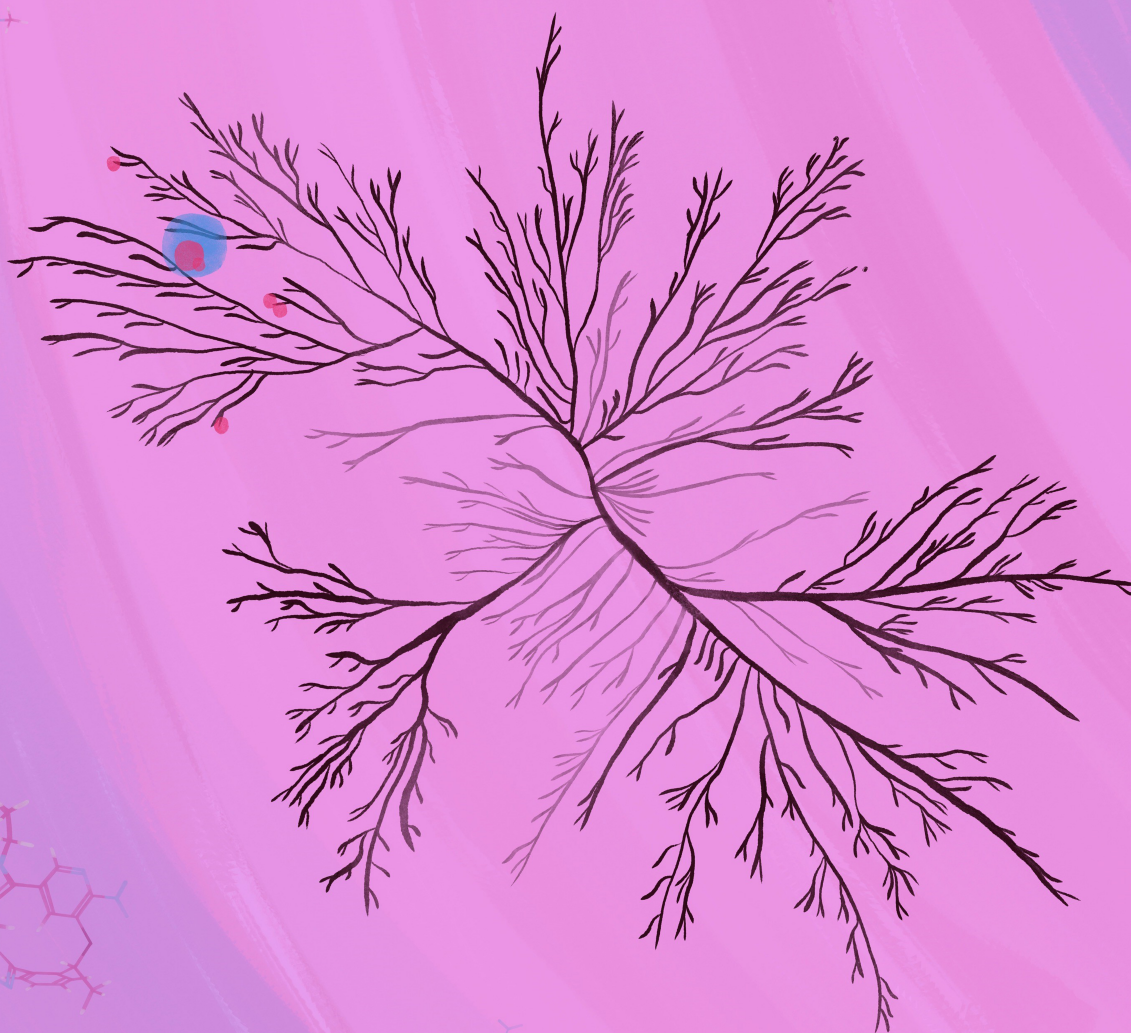


NVL-520 Is a Selective, TRK-Sparing, and Brain-Penetrant Inhibitor of ROS1 Fusions and Secondary Resistance Mutations

Alexander Drilon¹, Joshua C. Horan², Anupong Tangpeerachaikul², Benjamin Besse³, Sai-Hong Ignatius Ou⁴, Shirish M. Gadgeel⁵, D. Ross Camidge⁶, Anthonie J. van der Wekken⁷, Linh Nguyen-Phuong⁸, Adam Acker⁸, Clare Keddy^{9,10}, Katelyn S. Nicholson^{9,10}, Satoshi Yoda^{8,11}, Scot Mente², Yuting Sun², John R. Soglia², Nancy E. Kohl^{2,12}, James R. Porter², Matthew D. Shair², Viola Zhu², Monika A. Davare^{9,10}, Aaron N. Hata^{8,11}, Henry E. Pelish², and Jessica J. Lin^{8,11}



ABSTRACT

ROS1 tyrosine kinase inhibitors (TKI) have been approved (crizotinib and entrectinib) or explored (lorlatinib, taletrectinib, and repotrectinib) for the treatment of ROS1 fusion-positive cancers, although none of them simultaneously address the need for broad resistance coverage, avoidance of clinically dose-limiting TRK inhibition, and brain penetration. NVL-520 is a rationally designed macrocycle with >50-fold ROS1 selectivity over 98% of the kinome tested. It is active *in vitro* against diverse ROS1 fusions and resistance mutations and exhibits 10- to 1,000-fold improved potency for the ROS1 G2032R solvent-front mutation over crizotinib, entrectinib, lorlatinib, taletrectinib, and repotrectinib. *In vivo*, it induces tumor regression in G2032R-inclusive intracranial and patient-derived xenograft models. Importantly, NVL-520 has an ~100-fold increased potency for ROS1 and ROS1 G2032R over TRK. As a clinical proof of concept, NVL-520 elicited objective tumor responses in three patients with TKI-refractory ROS1 fusion-positive lung cancers, including two with ROS1 G2032R and one with intracranial metastases, with no observed neurologic toxicities.

SIGNIFICANCE: The combined preclinical features of NVL-520 that include potent targeting of ROS1 and diverse ROS1 resistance mutations, high selectivity for ROS1 G2032R over TRK, and brain penetration mark the development of a distinct ROS1 TKI with the potential to surpass the limitations of earlier-generation TKIs for ROS1 fusion-positive patients.

INTRODUCTION

ROS1 is an orphan receptor tyrosine kinase encoded by the *ROS1* proto-oncogene (1). Chromosomal rearrangements joining the 3' region of *ROS1*, which encodes the kinase domain, with the 5' region of partner genes produce constitutively active ROS1 fusion kinases. These fusions drive aberrant downstream signaling and transformation and are recurrent oncogenic drivers in human cancers (1). *ROS1* fusions are present in 1% to 3% of advanced non-small cell lung cancer (NSCLC), in which *CD74-ROS1* is the most prevalent fusion (2), and in other solid tumors such as cholangiocarcinoma (3), glioblastoma (4), angiosarcoma (5), and ovarian cancer (6). More than 50 *ROS1* fusion partners have

been identified (7), including *CD74*, *CEP85L*, *EZR*, *GOPC(L)*, *GOPC(S)*, *SDC4*, and *SLC34A2*. Each fusion partner may exert a different effect on subcellular localization, signaling, metastatic capacity, and drug sensitivity (8–10).

The tyrosine kinase inhibitors (TKI) crizotinib (11) and entrectinib (12) are approved by multiple regulatory agencies for the treatment of patients with TKI-naïve *ROS1* fusion-positive NSCLC. The National Comprehensive Cancer Network Clinical Practice Guidelines in Oncology list lorlatinib (13) as a treatment option for TKI-treated *ROS1* fusion-positive NSCLC (14). The investigational TKIs taletrectinib (15) and repotrectinib (16) are undergoing clinical evaluation for the treatment of *ROS1* fusion-positive cancers. Despite the availability of these options, each TKI has key deficiencies that can limit the likelihood and durability of therapeutic response.

Crizotinib has limited brain penetrance (17), an important deficiency given that 20% to 40% of patients with *ROS1* fusion-positive NSCLC present with central nervous system (CNS) metastases at diagnosis (18), and CNS metastases represent the sole site of progression in half of crizotinib-treated patients (19). Furthermore, the efficacy of crizotinib, entrectinib, and lorlatinib is limited by acquired mutations in the ROS1 kinase domain (20, 21). The G2032R “solvent-front” substitution, identified in 30% to 40% of patients after crizotinib or lorlatinib progression (20), is particularly recalcitrant. Other clinically observed *ROS1* resistance mutations include S1986F (22), S1986Y (22), F2004C (23), F2004I (21), F2004V (24), L2026M (25), D2033N (26), and G2101A (27).

Although responses to taletrectinib and repotrectinib have been reported in patients with tumors harboring ROS1 G2032R, both agents are associated with toxicities including gastrointestinal and neurologic adverse events (15, 28, 29). Many neurologic adverse events are attributed to the inhibition of tropomyosin-related kinases (TRK): TRKA, TRKB, and TRKC (30). Entrectinib, lorlatinib, taletrectinib, and repotrectinib inhibit both ROS1 and TRKA/B/C (12, 15, 31, 32) due to structural similarities between these kinases. TRKB inhibition

¹Memorial Sloan Kettering Cancer Center and Weill Cornell Medical College, New York, New York. ²Nuvalent, Inc., Cambridge, Massachusetts. ³Institut Gustave Roussy, Villejuif, France. ⁴University of California Irvine Medical Center, Orange, California. ⁵Henry Ford Cancer Institute, Detroit, Michigan. ⁶University of Colorado Cancer Center, Anschutz Medical Campus, Aurora, Colorado. ⁷University of Groningen, University Medical Centre Groningen, Groningen, the Netherlands. ⁸Massachusetts General Hospital Cancer Center, Charlestown, Massachusetts. ⁹Division of Pediatric Hematology/Oncology, Department of Pediatrics, Oregon Health and Science University, Portland, Oregon. ¹⁰Pap  Family Pediatric Research Institute, Oregon Health and Science University, Portland, Oregon. ¹¹Department of Medicine, Massachusetts General Hospital and Harvard Medical School, Boston, Massachusetts. ¹²Kohl Consulting, Wellesley, Massachusetts.

Note: A. Drilon, J.C. Horan, and A. Tangpeeraichauk contributed equally to this article.

Corresponding Authors: Henry E. Pelish, Nuvalent, Inc., One Broadway, 14th Floor, Cambridge, MA 02142. Phone: 617-872-5700; E-mail: hpelish@nuvalent.com; and Jessica J. Lin, 32 Fruit Street, Yawkey 7B, Boston, MA 02114. Phone: 617-724-1100; E-mail: jjlin1@partners.org
Cancer Discov 2023;13:598–615

doi: 10.1158/2159-8290.CD-22-0968

This open access article is distributed under the Creative Commons Attribution-NonCommercial-NoDerivatives 4.0 International (CC BY-NC-ND 4.0) license.

 2022 The Authors; Published by the American Association for Cancer Research

has been associated with cognitive impairment, mood/sleep disturbance, dizziness, ataxia, orthostasis, and weight gain—side effects that can be dose limiting and affect quality of life (33).

These experiences underscore the need for a ROS1 inhibitor that surpasses the limitations of earlier-generation agents. We describe the discovery of a novel ROS1-selective TKI, NVL-520. Preclinical characterization in biochemical assays, cell-based assays, and *in vivo* cancer models indicates that NVL-520 potently inhibits diverse ROS1 fusions and resistance mutations, is brain penetrant, and spares TRK inhibition. These preclinical findings are supported by three case studies presented here from an ongoing first-in-human study of NVL-520. Among these cases, which include two patients with detectable ROS1 G2032R, intracranial and/or extracranial RECIST 1.1 partial responses were observed in the absence of neurologic toxicities.

RESULTS

Design and Structure

NVL-520 is a macrocyclic small molecule (Fig. 1A). Computational modeling suggested that NVL-520 binds ROS1 in a manner similar to lorlatinib (PDB: 4UXL; ref. 34), with the aminopyridine moiety of NVL-520 forming two hydrogen bonds with Glu2027 and Met2029 in the hinge region (Fig. 1B). Besides binding ROS1, NVL-520 was rationally designed to address the three following medical needs.

Activity for ROS1 Resistance Mutations

The chemical structures of crizotinib, entrectinib, and lorlatinib have atoms that partially or fully occupy the solvent-front region of the binding pocket. Mutations in this region, particularly G2032R, have been hypothesized to cause a steric clash between protein and inhibitor, reducing TKI affinity and conferring TKI resistance (32, 35). NVL-520 was designed to minimize bulk in this region, potentially reducing steric clashes and thereby preserving affinity for ROS1 G2032R. Consistent with this design, free energy perturbation (FEP) calculations (36, 37) predicted larger binding energy shifts and ligand movement upon direct computational mutation of Gly2032 to arginine for crizotinib, entrectinib, and lorlatinib ($\Delta\Delta G_{\text{FEP}} \geq 3.6$ kcal/mol and $\Delta\text{RMSD} \geq 0.4$ Å) compared with NVL-520 ($\Delta\Delta G_{\text{FEP}} = 1.5$ kcal/mol and $\Delta\text{RMSD} = 0$ Å; Supplementary Fig. S1A and S1B). Additionally, FEP simulations revealed a hydrogen bond between the *N*-ethyl pyrazole of NVL-520 and Arg2032 (Fig. 1B). FEP results were further supported by biochemical assays and a resistant allele study (*vide infra*), as well as by predictions for repotrectinib that are consistent with its reported ROS1 G2032R activity (ref. 32; $\Delta\Delta G_{\text{FEP}} = 0.2$ kcal/mol and $\Delta\text{RMSD} = 0.1$ Å; Supplementary Fig. S1A and S1B).

Avoiding TRK Inhibition

The ROS1 TKIs entrectinib, taletrectinib, and repotrectinib cross-interact with TRK because of structural similarities between the kinases. Based on a crystal structure (PDB: 4UXL; ref. 34), amino acids that lie within 4.5 Å of the ROS1 ligand binding pocket have >70% identity with analogous residues on TRKA. To improve selectivity, we performed structural overlays and identified a potential differentiating residue at Leu2028 of ROS1, which corresponds to a sterically larger

tyrosine residue at the equivalent position in TRK (TRKA Y591, TRKB Y619, and TRKC Y619; Fig. 1C). The *N*-ethyl pyrazole of NVL-520 was found to potentially clash with the larger tyrosine residue in TRKA/TRKB/TRKC (Fig. 1C) while avoiding a negative interaction with the smaller Leu2028 in ROS1, which could result in preferential binding to ROS1 over TRK.

Brain Penetration

The physicochemical properties of NVL-520 (molecular weight: 419 g/mol; calculated $\log D_{7.4}$: 2.8; topological polar surface area: 97 Å²; predicted basic pKa: 5.7; and two hydrogen bond donors; Supplementary Fig. S1C) suggested that the compound exists within CNS drug chemical space. A CNS multiparameter score of 4.5 was derived, consistent with the potential for brain penetration and activity (38).

Biochemical Activity

Wild-type ROS1

Six ROS1 TKIs (crizotinib, entrectinib, lorlatinib, taletrectinib, repotrectinib, and NVL-520) were profiled in a biochemical phosphorylation assay using the purified wild-type ROS1 kinase domain. The assay was performed in the presence of 1 mmol/L ATP to simulate competitive inhibition against a physiologic ATP concentration. All compounds potently inhibited wild-type ROS1 ($IC_{50} = 0.3$ –12 nmol/L; Fig. 1D), with NVL-520 exhibiting subnanomolar potency ($IC_{50} = 0.7$ nmol/L; Fig. 1D; Supplementary Fig. S2A).

ROS1 G2032R

G2032R is the most frequent ROS1 substitution that confers clinical resistance to ROS1 TKIs after disease progression on crizotinib, entrectinib, or lorlatinib (20, 21). Consistent with these observations, purified ROS1 G2032R was resistant to crizotinib, entrectinib, and lorlatinib ($IC_{50} = 790$ –5,700 nmol/L; Fig. 1D), corresponding to a >100-fold loss in potency compared with wild-type ROS1 ($IC_{50} = 0.3$ –12 nmol/L). Taletrectinib and repotrectinib had moderate activity against ROS1 G2032R ($IC_{50} = 30$ –100 nmol/L). By contrast, NVL-520 demonstrated single-digit nanomolar potency against ROS1 G2032R ($IC_{50} = 7.9$ nmol/L), representing a potency improvement of 4-fold over repotrectinib ($IC_{50} = 30$ nmol/L), 13-fold over taletrectinib ($IC_{50} = 100$ nmol/L), and >100-fold over crizotinib, entrectinib, and lorlatinib ($IC_{50} = 790$ –5,700 nmol/L; Fig. 1D; Supplementary Fig. S2B). The biochemical potency shifts between wild-type ROS1 and ROS1 G2032R ($\Delta\Delta G_{\text{biochem}}$) correlated well with binding energy shifts predicted by FEP calculations ($\Delta\Delta G_{\text{FEP}}$; Supplementary Fig. S1B).

Kinome Selectivity

In a biochemical screen against 335 wild-type human kinase domains, NVL-520 was highly selective (Fig. 1E; Supplementary Fig. S3A). ROS1 was the most strongly inhibited target, followed by ALK which had 2-fold weaker IC_{50} than ROS1 (Supplementary Fig. S3B). Besides ALK, no other kinases were inhibited within 10-fold of the IC_{50} of NVL-520 for ROS1. NVL-520 had a >50-fold selectivity for ROS1 over 97.9% (328/335) of the tested kinome, with only five additional targets (LTK, FAK, PYK2, FER, and TRKB) inhibited with IC_{50} between 10- and 50-fold of ROS1 (Supplementary

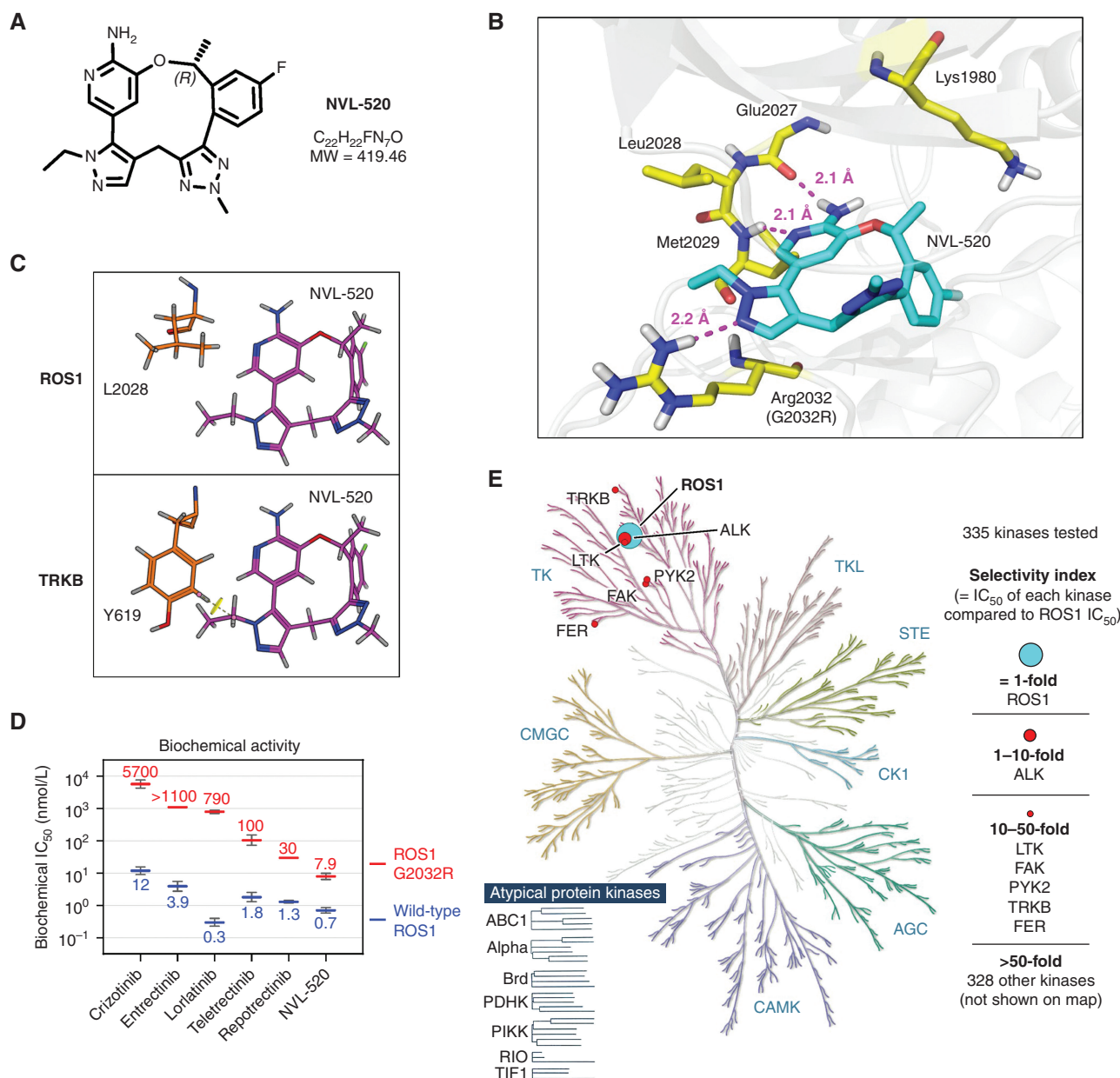


Figure 1. Design and biochemical activity of NVL-520. **A**, Chemical structure of NVL-520. MW, molecular weight. **B**, A snapshot from FEP simulations showing the model of NVL-520 (cyan) in the binding pocket of ROS1 G2032R, with key residues highlighted in yellow. Putative hydrogen bonding interactions and distances are shown in magenta. **C**, Structural overlay of NVL-520 (magenta) in the binding pockets of ROS1 and TRKB, based on the pose in **B**. Yellow disk indicates a steric clash between TRKB Tyr619 and NVL-520 based on van der Waals distance. **D**, Activity of six TKIs against ROS1 and ROS1 G2032R in biochemical assays. Geometric mean and standard deviation are plotted, with numerical values of the means shown (also see Supplementary Fig. S11A). **E**, Kinome selectivity tree for NVL-520. Seven kinases inhibited with IC₅₀ within 50-fold of ROS1 are indicated.

Fig. S3B). Because TRKB scored in this assay as a weak hit (IC₅₀ = 28-fold above ROS1) and was a key off-target of concern, we further profiled TRKB using additional assays (see the “Selectivity for ROS1 over TRK” section).

Cellular Activity

Six ROS1 TKIs (crizotinib, entrectinib, lorlatinib, taletrectinib, reprotrectinib, and NVL-520) were profiled in cell viability assays against a collection of two patient-derived cell lines, one human cancer cell line, and 18 engineered Ba/F3 cell

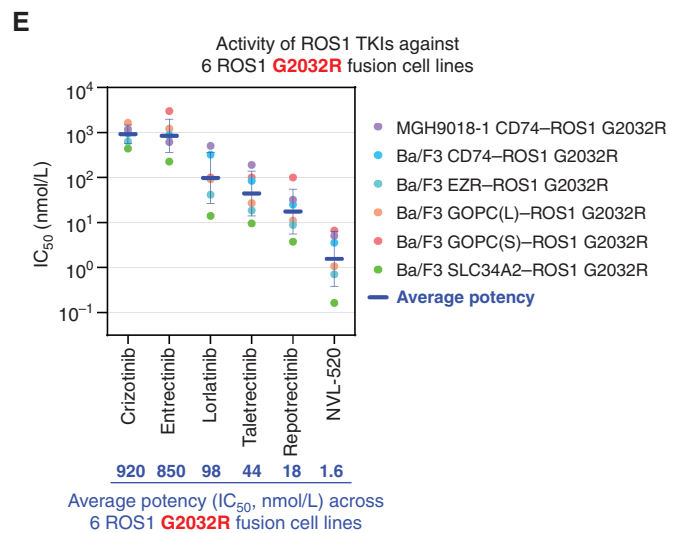
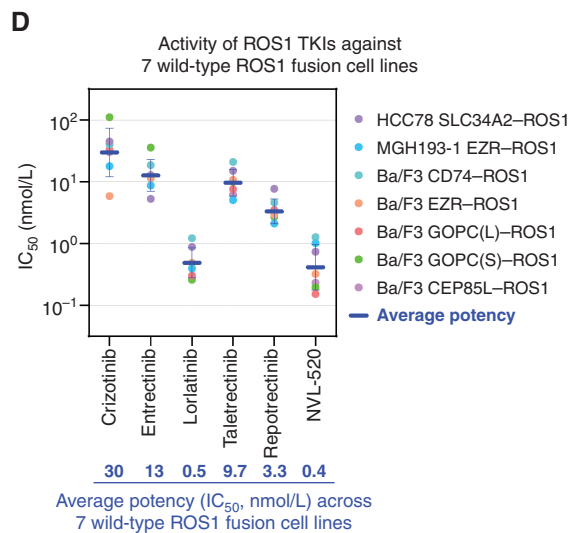
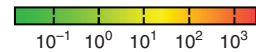
lines (Fig. 2A–C; Supplementary Fig. S4A and S4B). These cell lines encompassed six ROS1 fusion partners [SLC34A2, EZR, CD74, GOPC(L), GOPC(S), and CEP85L] and eight ROS1 mutational variants (wild-type, G2032R, S1986F, F2004C, F2004V, L2026M, D2033N, and G2101A).

Wild-type ROS1

In seven cell lines expressing wild-type ROS1 fusions, all six TKIs had growth inhibitory activity albeit with differing levels of potency (Fig. 2A and D). NVL-520 and lorlatinib

	Name	Cell line	Fusion	Mutation	Crizotinib	Entrectinib	Lorlatinib	Taletrectinib	Reprotrectinib	NVL-520	
A	HCC78	Human cancer cell line	SLC34A2-ROS1	—	45	5.3	0.9	15	7.7	<0.7	
	MGH193-1	Patient-derived cell line	EZR-ROS1	—	18	8.7	0.4	5	2.1	1	
	Wild-type ROS1 fusion	Ba/F3	Engineered mouse pro-B cell line	CD74-ROS1	—	40	19	1.2	21	4.6	1.3
				EZR-ROS1	—	5.9	12	0.5	11	2.9	0.3
				GOPC(L)-ROS1	—	33	11	0.3	7.6	3.5	0.2
				GOPC(S)-ROS1	—	110	36	0.3	9.9	2.7	0.2
				CEP85L-ROS1	—	30	13	0.4	6.2	2.1	0.2
Average potency across 7 wild-type ROS1 fusion cell lines					30	13	0.5	9.7	3.3	0.4	
B	MGH9018-1	Patient-derived cell line	CD74-ROS1	G2032R	1,100	610	500	190	32	5.1	
	ROS1 fusion with G2032R mutation	Ba/F3	Engineered mouse pro-B cell line	CD74-ROS1	G2032R	950	880	320	84	25	3.6
				EZR-ROS1	G2032R	630	830	42	19	8.8	0.7
				GOPC(L)-ROS1	G2032R	1,600	1,200	91	27	11	1.1
				GOPC(S)-ROS1	G2032R	1,200	>3,000	>100	>100	>100	6.6
				SLC34A2-ROS1	G2032R	440	220	14	9.4	3.8	0.2
Average potency across 6 ROS1 G2032R fusion cell lines					920	850	98	44	18	1.6	
C	ROS1 fusion with other resistance mutations	Ba/F3	Engineered mouse pro-B cell line	CD74-ROS1	S1986F	39	26	<0.3	NA	0.84	<0.6
				CD74-ROS1	F2004C	35	60	0.3	13	3.2	0.02
				EZR-ROS1	F2004C	28	66	0.5	13	3.5	0.01
				CD74-ROS1	F2004V	35	38	0.5	8.5	2.5	0.01
				EZR-ROS1	F2004V	11	51	0.6	10	3.6	0.2
				CD74-ROS1	L2026M	110	41	0.8	NA	3.3	1.5
				CD74-ROS1	D2033N	77	79	0.4	NA	2.5	1
				EZR-ROS1	G2101A	25	8.4	0.4	9.3	1.8	0.4

Cell viability IC₅₀ (nmol/L)



were the most potent (average IC_{50} = 0.4 nmol/L and 0.5 nmol/L, respectively; Fig. 2D), with potency exceeding that of repotrectinib by 7-fold (IC_{50} = 3.3 nmol/L) and that of crizotinib, entrectinib, or taletrectinib by >19-fold (IC_{50} = 9.7–30 nmol/L). To confirm that the antiproliferative activity of NVL-520 correlated with inhibition of ROS1 signaling, we measured ROS1 pathway activity in the MGH193-1 patient-derived cell line (EZR-ROS1). NVL-520 completely inhibited ROS1 autophosphorylation and downstream AKT/ERK signaling at 3 nmol/L, the lowest tested concentration (Supplementary Fig. S5A and S5B), supporting an on-target mechanism of action.

ROS1 G2032R

In six cell lines harboring ROS1 fusions with the G2032R mutation, NVL-520 was the only TKI to achieve single-digit nanomolar potency (average IC_{50} = 1.6 nmol/L; Fig. 2B and E), which exceeded repotrectinib and taletrectinib by >10-fold (IC_{50} = 18–44 nmol/L), lorlatinib by >60-fold (IC_{50} = 98 nmol/L), and crizotinib and entrectinib by >500-fold (IC_{50} = 850–920 nmol/L). Consistent with on-target activity, NVL-520 potently inhibited ROS1 signaling (Supplementary Fig. S5C and S5D) in the MGH9018-1 patient-derived cell line harboring CD74-ROS1 G2032R derived from a patient after crizotinib progression.

To measure the effects of G2032R substitution on TKI sensitivity, we analyzed the IC_{50} shifts from wild-type ROS1 to ROS1 G2032R for six TKIs in three matched fusion pairs (Supplementary Fig. S6). The analysis revealed two distinct groups of ROS1 TKIs based on their tolerance to G2032R. For the first group comprising crizotinib, entrectinib, and lorlatinib, G2032R caused an IC_{50} loss of 60- to 220-fold compared with wild-type ROS1, consistent with G2032R being observed in patients progressing on these drugs (20, 21). The second group comprising taletrectinib, repotrectinib, and NVL-520 was more tolerant of G2032R, showing an IC_{50} loss of 3- to 4-fold compared with wild-type ROS1 (Supplementary Fig. S6).

Other ROS1 Resistance Mutations

Besides G2032R, other substitutions observed after disease progression on crizotinib and/or entrectinib include S1986F, F2004C, F2004V, L2026M, D2033N, and G2101A (22–27). We expressed CD74-ROS1 or EZR-ROS1 fusion proteins harboring these mutations in Ba/F3 cells and tested them in cell viability assays against six TKIs. NVL-520 potently inhibited the non-G2032R ROS1 mutants with IC_{50} ≤ 1.5 nmol/L (Fig. 2C; Supplementary Fig. S7A). IC_{50} shift analysis revealed that most non-G2032R mutations caused ROS1 to become more resistant to crizotinib and entrectinib (Supplementary Fig. S7B), but the degree of resistance was modest (IC_{50} shift = 0.7–5.7-fold; Supplementary Fig. S7C, red box) and smaller in magnitude compared with G2032R (IC_{50}

shift = 24–110-fold). Conversely, the non-G2032R mutations did not confer resistance to lorlatinib, taletrectinib, repotrectinib, and NVL-520 (IC_{50} shift = 0.01–1.3-fold; Supplementary Fig. S7C, green box).

Fusion Partners

Given the diversity of upstream ROS1 fusion partners (7–10), we interrogated ROS1 TKIs in Ba/F3 cells expressing CD74-, EZR-, GOPC(L)-, GOPC(S)-, CEP85L-, or SLC34A2-ROS1 fusions, with a wild-type kinase domain or with the G2032R mutation. NVL-520 showed potent activity across all ROS1 fusions evaluated (IC_{50} < 10 nmol/L; Fig. 2D and E).

ROS1 On-Target Activity

We determined that the ROS1 L2086F mutation desensitized Ba/F3 cells to NVL-520, shifting its IC_{50} from 1.3 nmol/L for CD74-ROS1 to 6.8 μ mol/L for CD74-ROS1 L2086F (Supplementary Fig. S8A–S8C). ROS1 L2086F is an on-target resistance mutation observed in cancers from patients who progressed on lorlatinib (20). A steric clash was postulated between L2086F and lorlatinib based on a cocrystal structure of lorlatinib and ROS1 (PDB: 4UXL; ref. 20). The shift in potency observed with NVL-520 is consistent with this steric clash hypothesis. This drug-resistant allele indicates that the activity of NVL-520 in ROS1-driven cells is a consequence of direct pharmacologic inhibition of ROS1. NVL-520 also did not inhibit the growth of ROS1-independent cell lines including A549 (KRAS G12S lung carcinoma), A431 (EGFR-amplified epidermoid carcinoma), NCI-H1975 (EGFR L858R/T790M NSCLC), engineered Ba/F3 cells (EGFR L858R/T790M/C797S), and IL3-supplemented parental Ba/F3 cells (IC_{50} > 8.5 μ mol/L in all cases; Supplementary Fig. S8A), further supporting the activity of NVL-520 in ROS1-driven cells as on target. Consistent with kinome profiling, NVL-520 inhibited the viability of ALK fusion-positive cell lines (Supplementary Fig. S8A).

Anchorage-Independent Growth

Anoikis avoidance is a hallmark of cancer and is potentially indicative of migratory or metastatic propensity (39, 40). To study the effect of ROS1 inhibition on anoikis, we performed anchorage-independent colony formation assays in NIH3T3 cells expressing CD74-ROS1 or EZR-ROS1 fusions. ROS1-transformed NIH3T3 cells lost contact inhibition and formed colonies on soft agar. For NIH3T3 cells expressing wild-type ROS1 fusions, all ROS1 TKIs evaluated suppressed colony formation by >80% at ≤100 nmol/L, with NVL-520 and lorlatinib having the highest potency, followed by crizotinib and then entrectinib (Supplementary Fig. S9A–S9C). This potency trend correlated with the degree of target engagement and signaling modulation measured by Western blotting (Supplementary Fig. S9D and S9E). In contrast, for NIH3T3 cells expressing ROS1 fusions with

Figure 2. NVL-520 inhibits the viability of ROS1-driven cancer cell lines. **A–C**, Heat map showing the activity of TKIs in 3-day cell viability assays against wild-type ROS1 (**A**), ROS1 G2032R (**B**), or ROS1 with other resistance mutations (**C**). Numerical IC_{50} values (nmol/L) are provided. Each row represents a distinct cell line, with the identity of the ROS1 fusion partner and the resistance mutation (if applicable) indicated. “ IC_{50} <” and “ IC_{50} >” are treated as “ IC_{50} =” for heat map coloring. Grayed-out entries indicate data not available (NA). All data represent geometric mean IC_{50} or best-fit IC_{50} across $n \geq 2$ repeat testing. Errors and repeats are provided in Supplementary Fig. S4A. Average potencies for wild-type ROS1 and for ROS1 G2032R are presented as a separate row and highlighted in blue text, representing the geometric mean of IC_{50} s across cell lines. **D** and **E**, Plots of data in Fig. 2B (**D**) and Fig. 2C (**E**). For each TKI, individual dots represent the IC_{50} against distinct cell lines, and the horizontal bar represents average potency (geometric mean with geometric standard deviation).

G2032R, only NVL-520 was able to inhibit colony formation by $\geq 90\%$ at 100 nmol/L, whereas other TKIs (crizotinib, entrectinib, and lorlatinib) had weaker effects at the same concentration (Supplementary Fig. S10A–S10C). This potency trend was confirmed by pathway analysis (Supplementary Fig. S10D and S10E). Although we did not evaluate taletrectinib in the colony formation assay, Western blot analysis indicated that NVL-520 was more potent than taletrectinib in ROS1-driven NIH3T3 cells (Supplementary Fig. S9D and S10D), consistent with our observations in cell culture.

Selectivity for ROS1 over TRK

Avoiding TRK inhibition was a primary goal in designing NVL-520. TRK inhibitory potency was measured in biochemical, cell viability, and cellular phosphorylation assays. Rather than absolute potency, we focused our analysis on the relative potency between TRK and ROS1 and defined a “selectivity window” as the IC_{50} ratio of TRK to ROS1 (wild-type or G2032R). A selectivity window > 1 implied higher potency for ROS1 than TRK, whereas a selectivity window < 1 indicated higher potency for TRK than ROS1. We profiled six ROS1 TKIs and calculated their selectivity windows in the below three assays.

Biochemical Assay

TKIs were assayed against purified TRKA, TRKB, and TRKC kinase domains. Individual potency against each TRK and the average potency across three TRK proteins are shown in Supplementary Fig. S11A. Entrectinib, taletrectinib, and repotrectinib inhibited all three TRK proteins with equal or even greater potency than ROS1 (average TRK $IC_{50} < 5$ nmol/L), resulting in relatively narrow selectivity windows (range: < 0.0001 –2.6-fold; Supplementary Fig. S11B). NVL-520 and lorlatinib were not potent TRK inhibitors (average $IC_{50} = 130$ nmol/L). Although lorlatinib was selective for wild-type ROS1 over TRK, this selectivity window was lost in the presence of G2032R (decreased from 433-fold to 0.2-fold; Supplementary Fig. S11B). By contrast, NVL-520 demonstrated selectivity for both wild-type ROS1 and ROS1 G2032R over TRK (185-fold and 16-fold, respectively; Supplementary Fig. S11B).

Cell Viability Assay

We expressed oncogenic TPM3–TRKA, ETV6–TRKB, or ETV6–TRKC fusion proteins in Ba/F3 cells and used antiproliferative activity as a surrogate for TRK inhibition. Consistent with the results from the biochemical assays, NVL-520 was the only TKI to demonstrate selectivity for both wild-type ROS1 and ROS1 G2032R over TRK in cell viability assays (210-fold and 75-fold, respectively; Supplementary Fig. S12A and S12B).

Cellular Phosphorylation Assay

TRK-related neurologic toxicities are most consistent with the known functions of the TRKB signaling pathway (30, 33). We therefore developed an additional assay that uses Ba/F3 cells stably expressing full-length TRKB. Stimulation of this cell line with the brain-derived neurotrophic factor (BDNF) promotes TRKB autophosphorylation (pTRKB). Consistent with our results in biochemical and cell viability assays, NVL-520 only weakly inhibited cellular TRKB phosphorylation ($IC_{50} = 850$ nmol/L; Fig. 3A), affording a wide selectivity window for both wild-type ROS1 and ROS1 G2032R over

pTRKB (670-fold and 240-fold, respectively; Fig. 3B) that was not achieved with any other ROS1 TKI tested.

In Vivo Activity

Wild-type ROS1 Xenografts

In subcutaneous CTG-0848 (CD74–ROS1) and Lu01-0414 (SDC4–ROS1) xenograft models derived from patients with ROS1 fusion-positive NSCLC, NVL-520 induced tumor regression at all doses ≥ 0.2 mg/kg twice daily (b.i.d.), showing a 77% to 95% average reduction in tumor volume on day 20 or 28, respectively (Fig. 4A and B). Even at the lowest dose evaluated (0.04 mg/kg b.i.d., corresponding to a plasma-free drug concentration at dosing trough or $C_{min,free}$ of only 0.2 to 0.7 nmol/L; Supplementary Fig. S13A and S13B), NVL-520 suppressed tumor growth in both models (Fig. 4A and B), consistent with its subnanomolar *in vitro* potency. Maximal efficacy was achieved at 0.2 to 1 mg/kg b.i.d.; no additional tumor suppression was observed at higher doses (Fig. 4A and B). At maximally efficacious doses of 5 and 15 mg/kg b.i.d. of NVL-520, treatment was continued until day 42, followed by treatment withdrawal and monitoring for an additional 42 days. Tumor volumes continually declined in both models during the 42 days of NVL-520 treatment. After treatment cessation, tumor volumes continued to be suppressed in the CTG-0848 model but increased in the Lu01-0414 model (Supplementary Fig. S13C and S13D).

Western blot analysis of tumor samples confirmed ROS1 inhibition *in vivo*, supporting an on-target mechanism of action (Supplementary Fig. S13A and S13B). NVL-520 promoted PARP cleavage, a marker of tumor cell apoptosis (Supplementary Fig. S13B), and induced a reduction in total ROS1 after 5 days of dosing (Supplementary Fig. S13A and S13B) in agreement with a previous report (41). Plasma drug concentrations upon a single dose or short-term repeat dosing (b.i.d. $\times 5$ days) were similar, and drug exposure increased linearly between the two doses examined (5 mg/kg yielded plasma drug concentrations approximately 100-fold that of the 0.04 mg/kg dose; Supplementary Fig. S13A and S13B). Plasma drug concentrations at different doses and time points correlated with the degree of ROS1 inhibition (Supplementary Fig. S13A and S13B).

ROS1 G2032R Xenografts

CTG-2532 and MGH9018-1 xenograft models were established from patients with NSCLC after crizotinib relapse; both patient-derived xenografts (PDX) harbor CD74–ROS1 with the G2032R resistance substitution. In both models, NVL-520 induced near-maximal regression at 5 mg/kg b.i.d., with an 88% to 94% average reduction in tumor volume (Fig. 4C and D). Western blot analysis revealed exposure-dependent ROS1 inhibition in tumors similar to that seen with our wild-type ROS1 xenografts, supporting on-target activity (Supplementary Fig. S14A and S14B). Furthermore, NVL-520 induced regression in the Ba/F3 CD74–ROS1 G2032R xenograft model that displayed a highly aggressive tumor growth behavior (13-fold tumor volume increase over 14 days in the vehicle group; Fig. 4E). No meaningful reductions in body weight were observed for NVL-520 in any of the studies at doses ranging from 0.04 to 15 mg/kg b.i.d. (Supplementary Fig. S15A–S15E). Taken together, our studies demonstrated the strong *in vivo* efficacy of NVL-520 against tumors driven by ROS1 fusions with or without the G2032R resistance substitution.

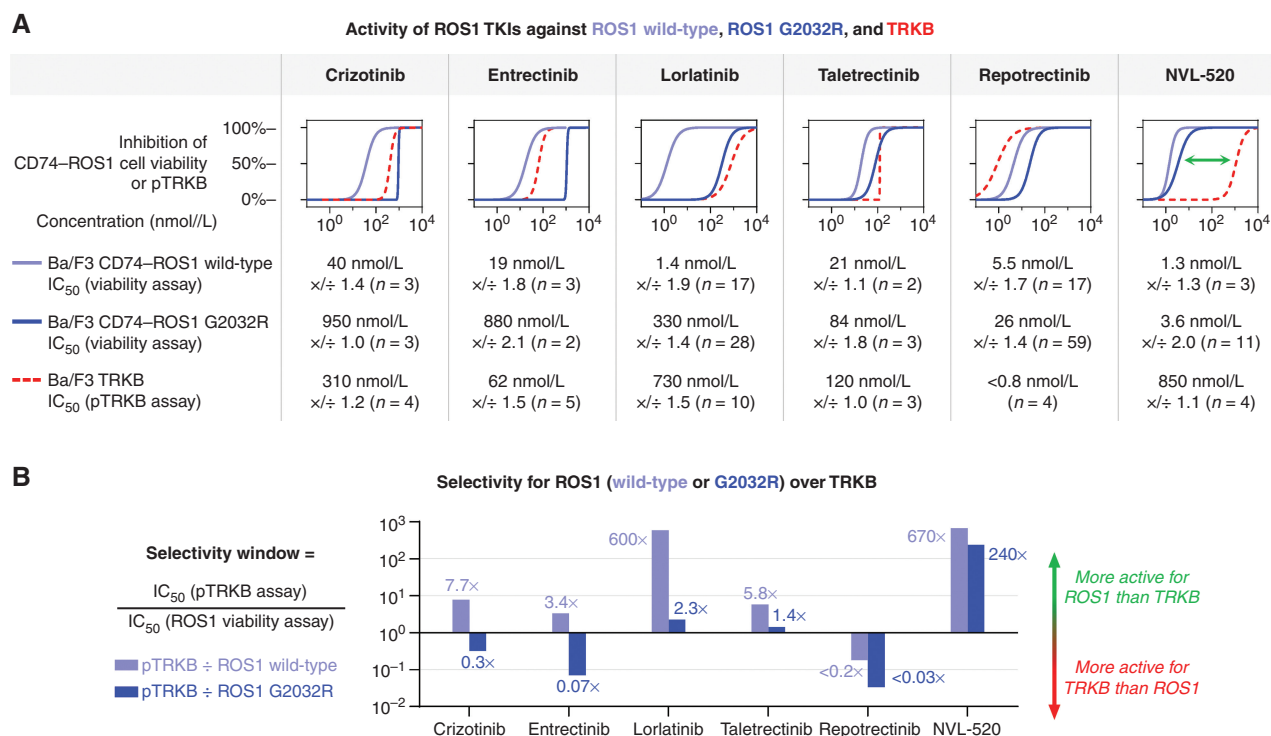


Figure 3. NVL-520 selectively inhibits ROS1 while avoiding pTRKB inhibition. **A**, Activity of ROS1 TKIs at inhibiting viability of ROS1 fusion cell lines or pTRKB in BDNF-stimulated Ba/F3 TRKB cells. pTRKB was measured with the AlphaLISA assay and was not normalized to total TRKB. Top, dose-response curve overlays highlighting the differential activity of ROS1 TKIs against ROS1, ROS1 G2032R, and pTRKB. The green arrow denotes the separation between ROS1 inhibition and TRKB inhibition of NVL-520. Curves are fitted to composite data from multiple repeats ($n \geq 2$), with individual datapoints not shown. Bottom, geometric means of IC₅₀ (nmol/L) with standard deviation and number of repeats are provided. **B**, Selectivity window analysis showing the relative preferences of each TKI for ROS1 or ROS1 G2032R over TRKB. Numerical selectivity values are indicated alongside the bars and are calculated from IC₅₀ values in **A**.

In the CTG-2532 and Ba/F3 xenograft models harboring CD74-ROS1 G2032R, we included repotrectinib treatment groups at 15 and 75 mg/kg b.i.d. following previously reported doses (32). Repotrectinib was not as efficacious or well tolerated as NVL-520 in the CTG-2532 model; it achieved tumor stasis at 15 mg/kg b.i.d. for most of the treatment period (Fig. 4D) but was not tolerated at 75 mg/kg b.i.d., as evidenced by a rapid ~20% body weight loss from days 6 to 13 (Supplementary Fig. S15D; no animals survived to the day 17 time point). However, both doses of repotrectinib induced regression in the Ba/F3 model (Fig. 4E). Of note, different mouse strains were utilized in the CTG-2532 model (athymic Nude-Foxn1nu mice) and the Ba/F3 model (Balb/c nude mice).

Preclinical Intracranial Activity

NVL-520 exhibited a $K_{p,uu}$ (unbound brain-to-plasma partitioning) of 0.16 measured at 1 hour after a single oral 10 mg/kg dose in Wistar Han rats, which was comparable to that of lorlatinib ($K_{p,uu} = 0.11$ in the same assay), a TKI with high CNS penetration (42–44). To assess intracranial antitumor activity, we generated a Ba/F3 CD74-ROS1 G2032R luciferase model that permitted monitoring of the brain tumor burden via live-animal bioluminescence imaging. We intracranially injected Ba/F3 CD74-ROS1 G2032R luciferase cells into mice and observed rapid tumor growth (Fig. 5A and B). All vehicle-treated mice lost body weight (Supplementary Fig. S15F) and succumbed to

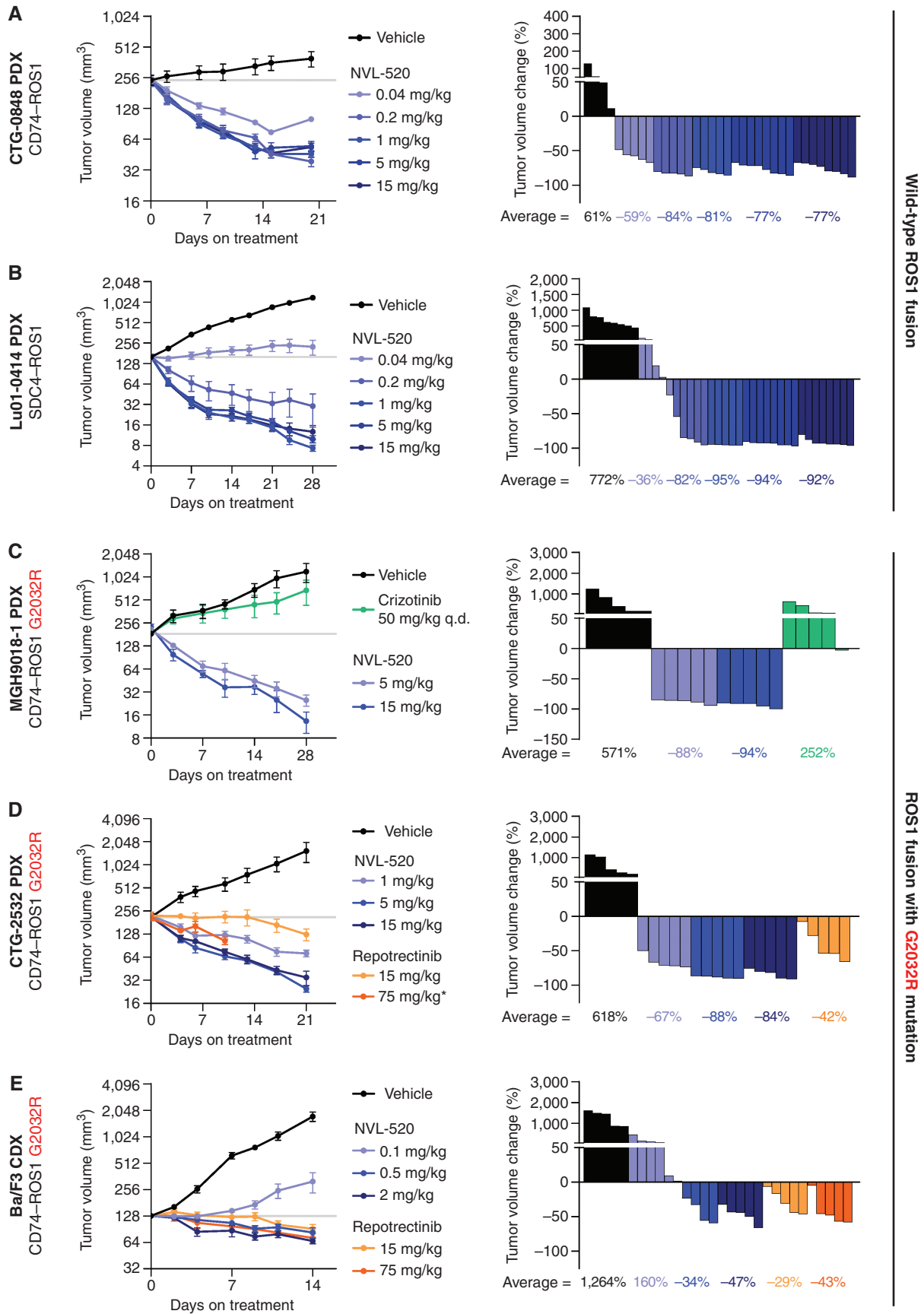
disease by day 19 with a median overall survival (mOS) of 16.5 days (Fig. 5C). In contrast, NVL-520 at 2 mg/kg suppressed intracranial tumor growth, with mean body weight loss <10% and all mice surviving to study termination (mOS > 61 days), corresponding to a >4-fold survival extension over vehicle treatment (Fig. 5A–C; Supplementary Fig. S15F). These results indicated that NVL-520 had intracranial antitumor activity.

Proof-of-Concept Clinical Activity

In the ongoing dose-escalation portion of the ARROS-1 first-in-human study of NVL-520, intracranial and extracranial activity has been observed in patients with TKI-pre-treated ROS1 fusion-positive NSCLC with and without the G2032R mutation (45).

Case Study 1

A 54-year-old patient with metastatic lung adenocarcinoma that responded to two cycles of carboplatin, paclitaxel, bevacizumab, and atezolizumab tested positive for ROS1 fusion by fluorescence *in situ* hybridization on tumor tissue. The patient received crizotinib for 2 months, complicated by pneumonitis, and subsequently received lorlatinib with an initial partial response (PR). Intrathoracic disease progression followed after 32 months. She then received two cycles of carboplatin and pemetrexed with continued lorlatinib and had stable disease. Next-generation sequencing (NGS)



of a lorlatinib-resistant lung nodule revealed a *CD74-ROS1* fusion with *ROS1* G2032R. The patient initiated NVL-520 at the lowest dose level of 25 mg once daily (q.d.). A clinical response was achieved within 2 weeks of therapy, with marked improvement in the patient's dyspnea. Imaging after 4 weeks showed a PR with a decrease in multiple bilateral lung metastases (−31% by RECIST 1.1), consistent with the plasma exposure level of NVL-520 (Supplementary Fig. S16A and S16B). The patient's NVL-520 dose was escalated to 75 mg q.d. after 8 weeks as permitted by the protocol, and she remained on therapy for approximately 6 months with an ongoing confirmed PR (−60% by RECIST 1.1; Fig. 6A) and with no reported neurologic toxicities as of the data cutoff.

Case Study 2

In addition to extracranial antitumor activity, intracranial activity was observed in another patient with metastatic NSCLC harboring *EZR-ROS1* G2032R. A 65-year-old patient with stage IV lung adenocarcinoma and multiple brain metastases had *EZR-ROS1* identified by circulating tumor DNA (ctDNA) testing. Entrectinib was initiated with an initial response, but the patient's disease progressed 9 months later. A biopsy of a growing liver lesion confirmed the known *EZR-ROS1* fusion and identified a *ROS1* G2032R mutation. The patient was transitioned to a clinical trial of repotrectinib. The patient quickly required a change in systemic therapy due to progressive disease and began a combination of carboplatin, pemetrexed, bevacizumab, and entrectinib. Unfortunately, a mixed response, growing brain metastases, and new liver metastases were observed. Repeat ctDNA testing again detected *ROS1* G2032R. NVL-520 was initiated at 50 mg q.d. At week 4, regression of a right occipital lobe metastasis was observed in addition to a decrease in several metastases in the liver and lung (−38% by RECIST 1.1), consistent with the plasma exposure level of NVL-520 and a reduction in allele frequencies of *EZR-ROS1* and *ROS1* G2032R by ctDNA (Supplementary Fig. S16A–S16C). The NVL-520 dose was escalated to 75 mg q.d. after 12 weeks. She remained on therapy at approximately 5 months with a confirmed PR, further disease regression in the brain and liver (−58% by RECIST 1.1; Fig. 6B), and no reported neurologic toxicities as of the data cutoff.

Case Study 3

The antitumor activity of NVL-520 extended to a case without known *ROS1* resistance mutations. A 75-year-old patient with a metastatic *EZR-ROS1* fusion-positive lung adenocarcinoma was initially treated by a referring physician with alectinib, an ALK TKI. Primary progression was observed, and treatment was transitioned to crizotinib. A clinical and radiologic response was maintained until 39 months, when bilateral growing lung nodules were noted on imaging. ctDNA analysis did not reveal any *ROS1* kinase domain mutations. NVL-520 was initiated at 25 mg q.d. and escalated to 75

mg q.d. after 24 weeks. Treatment was well tolerated with no evidence of dizziness, orthostasis, or paresthesia. A PR (−33% by RECIST 1.1), consistent with the plasma exposure level of NVL-520, was observed at week 4; this was confirmed and maintained with ongoing treatment of approximately 8 months (−48% by RECIST 1.1; Supplementary Fig. S16A, S16B, and S16D) as of the data cutoff.

DISCUSSION

TKIs have achieved increasing success in oncogene-driven cancers due to generational improvements in rational drug design. In metastatic disease, coverage of on-target resistance and increased intracranial activity have enabled sequential TKI therapy paradigms, whereby a later-generation TKI can reestablish disease control after progression on an early-generation TKI. Importantly, later-generation TKIs have replaced early-generation TKIs as care standards in metastatic, treatment-naïve *EGFR*-mutant and *ALK* fusion-positive lung cancers due to improvements in durable disease control (46, 47). Increased tolerability is a critical design feature that permits longer term dosing.

A structure-based approach was used to design NVL-520, a novel, brain-penetrant *ROS1* TKI that is generationally distinct from other *ROS1* TKIs. NVL-520 combines the advantages of potent inhibition of *ROS1* G2032R resistance mutation with limited TRK inhibition, resulting in increased selectivity for *ROS1* G2032R over TRK compared with other *ROS1* TKIs. By minimizing clashing interactions and forming a putative positive interaction in the solvent-front region, NVL-520 retains single-digit nanomolar potency against diverse *ROS1* fusions and *ROS1* kinase domain resistance substitutions. NVL-520's potency exceeded that of approved or investigational agents (crizotinib, entrectinib, lorlatinib, taletrectinib, and repotrectinib) by 1 to 3 orders of magnitude for *ROS1* G2032R. This strategy for targeting *ROS1* solvent-front resistance parallels the recent report of a lorlatinib analogue (LA9) with preclinical activity against *ALK* solvent-front resistance resulting from a productive interaction hypothesized between its lactam carbonyl and *ALK* G1202R (48). Identification of the *ROS1* L2086F mutation that confers resistance to NVL-520 *in vitro* is consistent with direct *ROS1* pharmacologic inhibition by NVL-520 and modeling of NVL-520 binding to *ROS1*. It also suggests that on-target resistance to NVL-520 may emerge in the clinic.

The biochemical and cellular profiles of NVL-520 translated into potent antitumor activity across a diverse range of *ROS1* fusion-driven preclinical models, including PDXs, with and without the recalcitrant *ROS1* G2032R mutation. Tumor regressions were evident in all models, and on-target activity was supported by measured reductions in phospho-*ROS1*. Concordant with these results, NVL-520 induced partial responses in three patients reported here with TKI-refractory,

Figure 4. NVL-520 inhibits *ROS1*-driven tumor xenografts. **A–E**, For each model, the change in tumor volume over time (left, plotted as mean ± SEM, with horizontal gray lines denoting mean starting tumor volume of the vehicle group) and a waterfall plot showing tumor volume changes from day 0 to the final time point shown (right) are provided. Average tumor volume changes are provided underneath the waterfall plots. For **A** and **B**, data are shown up to days 20 and 28, respectively; longer treatments are provided in Supplementary Fig. S13C and S13D. MGH9018-1 was confirmed to be crizotinib-resistant (**C**). *For 75 mg/kg repotrectinib, day 10 is the last reported datapoint due to lack of tolerability and loss of animals after day 10 (**D**). Each group contained 4 to 8 mice. All treatments were administered orally b.i.d. unless otherwise indicated. CDX, cell line-derived xenograft; q.d., once daily.

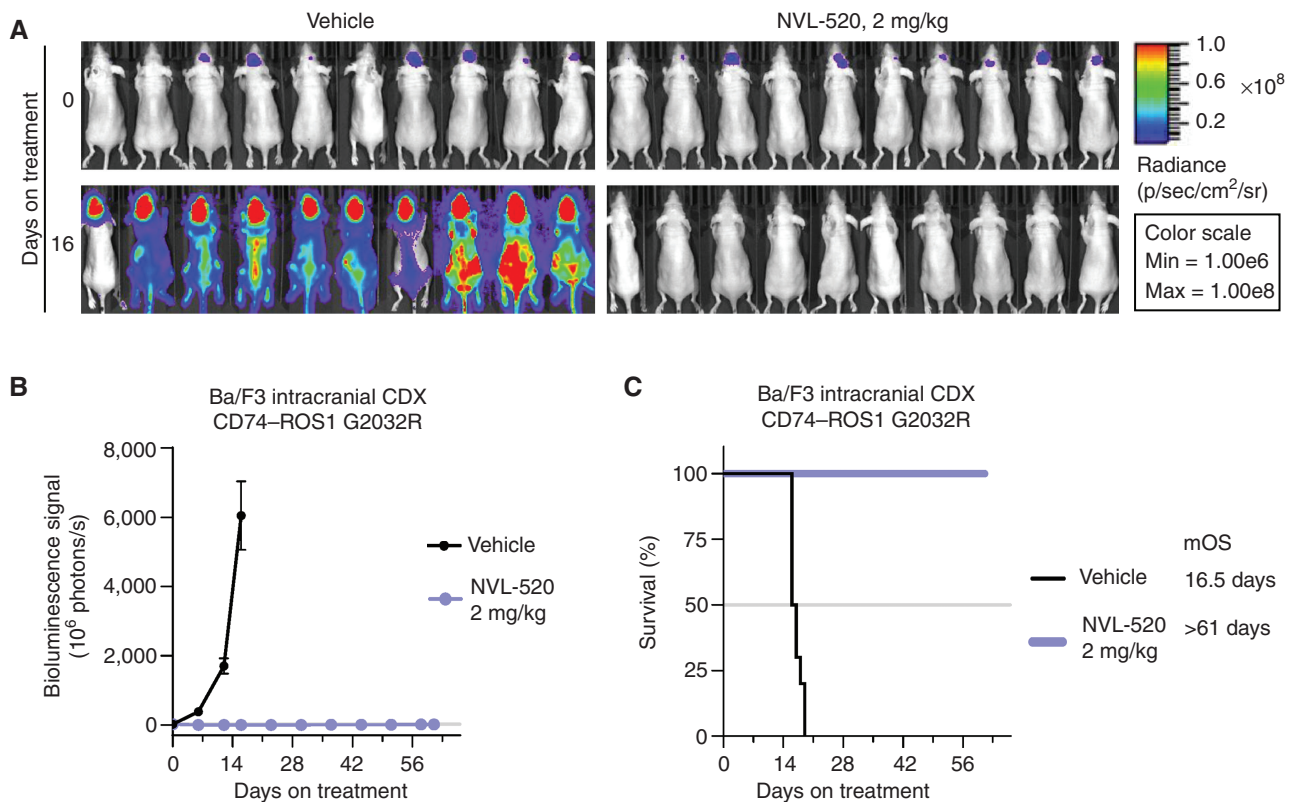


Figure 5. NVL-520 inhibits the growth of an intracranial ROS1-driven tumor xenograft. **A**, Bioluminescence images indicating a change in tumor burden over 16 days of treatment. **B**, A plot of intracranial bioluminescence over time. **C**, Survival analysis with mOS indicated. Each group contained 7 to 10 mice. All treatments were administered orally b.i.d. CDX, cell line-derived xenograft.

ROS1 fusion-positive NSCLCs. Importantly, these confirmed responses were achieved with tumors refractory to a wide generational variety of ROS1 TKIs (i.e., crizotinib, entrectinib, lorlatinib, and repotrectinib).

NVL-520 was specifically designed to address the competing challenges of potent ROS1 G2032R inhibition and the avoidance of TRK inhibition—either or both of which represent liabilities associated with existing ROS1 inhibitors. As an example, although repotrectinib inhibits ROS1 G2032R (49), it was initially designed to treat ROS1-, ALK-, and TRK-driven tumors, including ALK and TRK G-to-R solvent-front mutants analogous to ROS1 G2032R. Such multikinase activity may be acceptable for targets such as ROS1 or ALK without substantial known on-target toxicities. Unfortunately, it is problematic when it includes targets such as TRK with dose-limiting on-target toxicities. Potential TRK-related toxicities reported for repotrectinib include dizziness, dysgeusia, paresthesia, and ataxia (32, 50). Furthermore, 34% and 10% of patients had treatment-emergent adverse events that led to dose reduction and discontinuation, respectively (29). TRK inhibition represents a liability that is also evident in the safety profiles of entrectinib, lorlatinib, and taletrectinib (44, 51, 52).

To limit TRK inhibition, NVL-520 was designed to present an *N*-ethyl substituent to clash with TRKA Y591 and TRKB/C Y619, a feature that also improves broad kinome selectivity as 60% of kinases contain a tyrosine at this hinge-preceding residue (43). NVL-520 has an approximately 100-fold increased

potency for ROS1 and ROS1 G2032R over TRK *in vitro*. Such a differential in effective concentrations may enable the selection of a clinical dose of NVL-520 that would fully inhibit diverse TKI-sensitive and TKI-resistant ROS1-driven tumors without significantly inhibiting endogenous TRK in the CNS, hence providing the potential for efficacy without inducing TRK-related neurologic toxicities. Consistent with its selectivity for ROS1 and against TRK, NVL-520 did not induce TRK-associated neurologic toxicities in the patients in this report, such as dizziness or ataxia.

Because *de novo* (18) and acquired (19) CNS metastases are frequent limiting factors in patients with ROS1 fusion-positive lung cancers and primary brain tumors or other cancers that metastasize to the CNS harbor ROS1 fusions (1), brain penetrance was a key design goal for NVL-520. The drug was efficacious in an intracranial model of CD74-ROS1 G2032R, providing a >4-fold mOS extension relative to vehicle. In keeping with these results, intracranial activity was observed at 4 weeks and maintained thereafter in a patient with a ROS1 fusion and G2032R mutation-positive NSCLC refractory to entrectinib (a drug with putatively improved CNS penetrance compared with crizotinib), repotrectinib, and platinum doublet chemotherapy.

Since the discovery of oncogenic ROS1 fusions in lung cancer in 2007 (53), our collective understanding of optimal ROS1 targeting has continued to evolve with each generation of ROS1 inhibitors. In the landscape of currently available

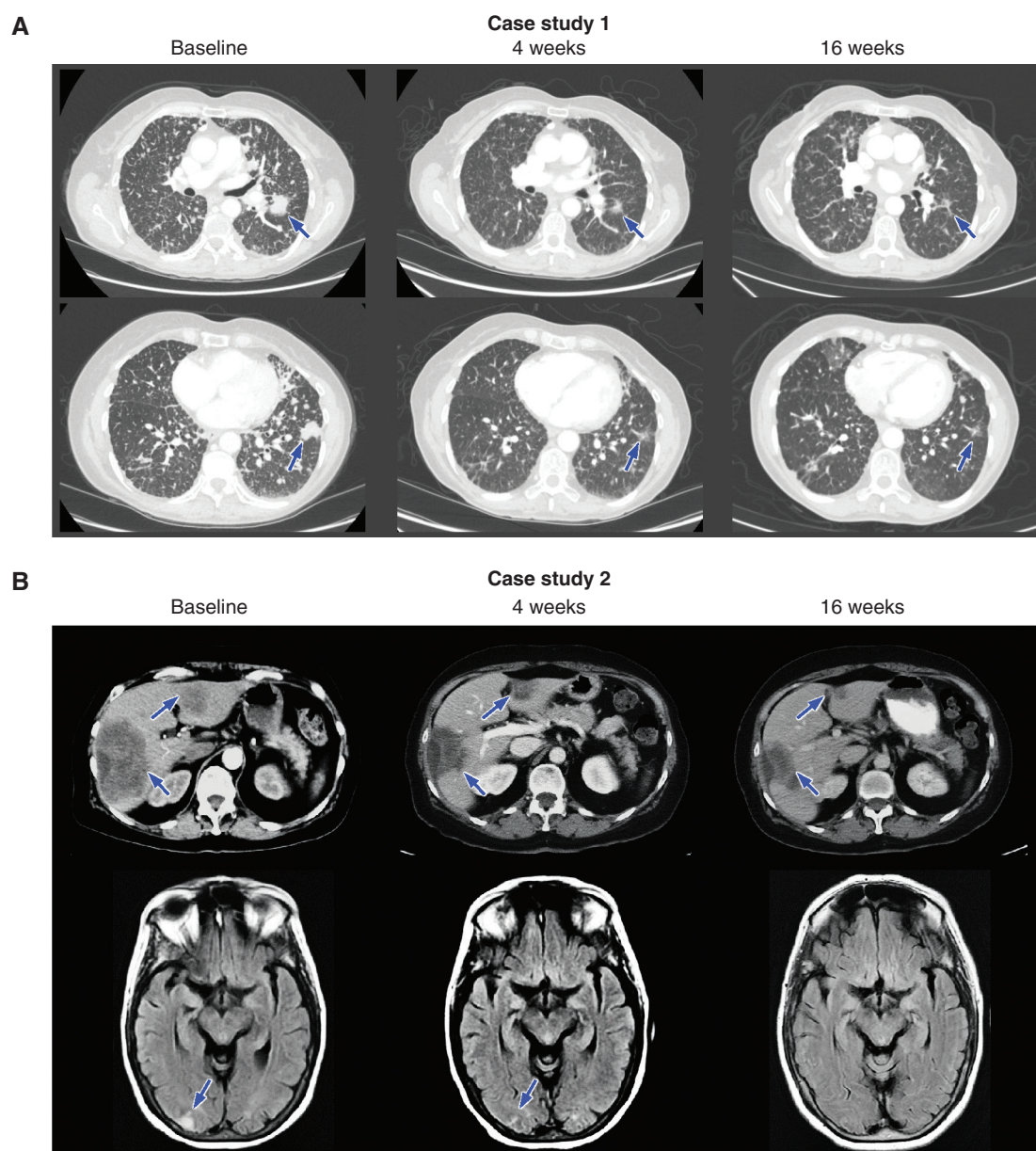


Figure 6. Clinical activity of NVL-520. **A**, Representative CT images demonstrating a confirmed PR to NVL-520 in a patient with *CD74-ROS1* fusion-positive lung adenocarcinoma with a *ROS1* G2032R resistance mutation after prior crizotinib, lorlatinib, and chemotherapy. The patient started at 25 mg q.d. of NVL-520 and then increased to 75 mg q.d. at 8 weeks. Blue arrows indicate left lung nodules that decreased in size over the course of treatment. **B**, Representative CT (top) and MRI (bottom) images demonstrating a confirmed PR to NVL-520 in a patient with *EZR-ROS1* fusion-positive lung adenocarcinoma with a *ROS1* G2032R resistance mutation after prior entrectinib, repotrectinib, and chemotherapy. The patient started at 50 mg of NVL-520 and then escalated to 75 mg at 12 weeks. Blue arrows in the top panel indicate segment 5/6 and 3 liver metastases with continuous regression over the course of treatment. Blue arrows in the bottom panel indicates a right occipital lobe metastasis that decreased in size at week 4 and became barely appreciable at week 16.

ROS1 TKIs, NVL-520 offers best-in-class features that are anchored in selectivity, resistance mutation coverage, and CNS penetrance. These features have the potential to improve outcomes in patients with *ROS1* fusion-positive tumors, and the early reports of clinical activity presented here and elsewhere (45) are highly encouraging. The ongoing ARROS-1 clinical trial, inclusive of a basket trial strategy, will further define the potential benefit of NVL-520 in patients with

advanced *ROS1* fusion-positive NSCLCs and other *ROS1* fusion-positive cancers (45).

METHODS

Compounds

Reference compounds were purchased from commercial sources: crizotinib (Combi-Blocks, #QE-4059; MedChemExpress, #HY-50878;

SelleckChem), entrectinib (Ark Pharm Inc., #AK547001; Advanced Chemblocks, #K13380; SelleckChem), talrectinib (MedChemExpress, #HY-131003), repotrectinib (Ark Pharm Inc., #AK689211; MedChemExpress, #HY-103022; SelleckChem, #S8583; DC Chemicals, #DC10463), and lorlatinib (Ark Pharm Inc., #AK175603; eNovation Chemicals, #Y0975931; SelleckChem). NVL-520 was identified from a structure-activity relationship (SAR) effort to discover kinase inhibitors potent against wild-type and mutant ROS1 and selective against the TRK family of receptor tyrosine kinases. Refer to the International Patent Application Publication WO 2021/226208, Example 5, for the synthetic preparation of NVL-520. Calculator Plugins were used for structure property prediction and calculation, Marvin 19.20.0, 2019, ChemAxon (<http://www.chemaxon.com>); $\log D_{7.4}$, topological polar surface area, and predicted basic pKa.

Computational Modeling

Sequence Similarity. ROS1 and TRKA pocket sequence identity was calculated by selecting the residues that are in proximity (4.5 Å) to the ligand in the 4UXL structure of ROS1. There are 21 residues in this set (ROS1: LGVEAKLLELMEGGDRNCLGD) compared with the analogous residues on TRKA (TRKA: LGVLAKVFEYMKHGDRNCLGD) obtained through Clustal Omega sequence alignment. Of the 21 residues in ROS1 and TRKA, 15 (71.4%) are identical and 16 (76.2%) are similar using the following similarity grouping: GAVLI, FYW, CM, ST, KRH, DENQ, P.

System Preparation for FEP⁺ Calculations. The initial modeling orientation of NVL-520 was prepared using the MOE docking protocol into the 4UXL structure of ROS1 (34). Model orientations of the other ligands were obtained by direct superposition of the published crystal structures of those ligands in ROS1 [lorlatinib: 4UXL (34); crizotinib: 3ZBF (35)], ALK (entrectinib: 5FTO; ref. 54), or TRKA (repotrectinib: 7VKN; ref. 55) onto the 4UXL structure. These superpositions were created using the default protein preparation wizard in Maestro 13.3 and served as the starting point for the subsequent FEP⁺ calculations. This preparation included adding hydrogens, filling missing side chains, and assigning proper ionization states for the amino acids and the ligands at physiologic pH. Prior to running the FEP⁺ simulations, missing ligand torsion parameters for all compounds were computed with the Force Field Builder that utilized the M06-2X/cc-pVTZ9(-f) functional. Crizotinib and entrectinib were simulated in their cation form with a +1 charge.

FEP⁺ Calculations. FEP⁺ (36) in the 2022–3 release with the OPLS4 force field (56) was used to predict the relative binding free energies for the ROS1–ligand complexes. A detailed description of the FEP⁺ methodology (36, 37, 57–59) and its use to predict ligand selectivity (60, 61) have been reported. The Desmond molecular dynamics calculations and FEP⁺ processing of results were accomplished on the Schrodinger-hosted AWS GPU server. During these calculations, the atoms of the arginine side chain were grown via the windowed perturbation scheme from glycine. Default values of 5 nanoseconds per lambda window and 24 lambda windows were used.

The Pose of NVL-520 in TRKB. The snapshot of NVL-520 in ROS1 from FEP simulations was used as a starting point. TRKB (PDB: 4AT3, ref. 62) was superimposed using the Schrodinger Maestro binding-site alignment protocol to illustrate the proximity between NVL-520 and TRKB Y619. NVL-520 was not separately docked onto TRKB.

Biochemical Kinase Activity Assay

Activity of purified kinases was measured using the PhosphoSens assay (AssayQuant Technologies; ref. 63). Test compounds were dissolved in DMSO to 100-fold over the desired concentration

and dispensed at 250 nL into a 384-well plate in a 3-fold dilution series. A 12.5 μ L solution containing 2 mmol/L ATP with 26 μ mol/L fluorogenic peptide substrate AQT0101 (AssayQuant Technologies, #AQT0101) or AQT0104 (AssayQuant Technologies, #AQT0104) in buffer (50 mmol/L HEPES pH 7.5, 0.01% Brij-35, 0.5 mmol/L EGTA, 10 mmol/L MgCl₂) was added to the plate. The reaction was triggered by the addition of a 12.5 μ L solution containing 0.5 nmol/L ROS1 (Carna, #08-163), 2 nmol/L ROS1 G2032R (SignalChem, #R14-12BG), 1 nmol/L TRKA (BPS Bio, #40280), 3 nmol/L TRKB (SignalChem, #N17-11G), or 0.5 nmol/L TRKC (BPS Bio, #40282) kinase domains in buffer (50 mmol/L HEPES pH 7.5, 0.01% Brij-35, 2% glycerol, 0.4 mg/mL BSA, 0.5 mmol/L EGTA, 10 mmol/L MgCl₂). The final concentrations were 1 mmol/L ATP, 13 μ mol/L peptide substrate (AQT0101 for ROS1 and ROS1 G2032R or AQT0104 for TRKA, TRKB, and TRKC), 0.25 to 1.5 nmol/L kinase (0.25 nmol/L ROS1; 1 nmol/L ROS1 G2032R; 0.5 nmol/L TRKA; 1.5 nmol/L TRKB; or 0.5 nmol/L TRKC), 50 mmol/L HEPES pH 7.5, 0.01% Brij-35, 1% glycerol, 0.2 mg/mL BSA, 0.5 mmol/L EGTA, and 10 mmol/L MgCl₂. The plate was sealed, and fluorescence signal was recorded by a plate reader at $\lambda_{\text{emission}} = 485$ nm every 2 minutes for 120 minutes at 30°C. The change in fluorescence intensity over time during the initial, linear phase of the reaction is initial velocity (v). IC₅₀ was calculated from the plot of initial velocity versus log (inhibitor concentration) regressed to the four-parameter logistic equation.

Kinase Panel Screening

Inhibition of kinase activity was measured using radiolabeled [γ -³³P]-ATP (Reaction Biology). A solution containing [γ -³³P]-ATP was mixed with NVL-520, each of the 335 kinases, and the corresponding kinase substrate. NVL-520 was assayed at two concentrations: 100 nmol/L and 1 μ mol/L. The concentration of ATP in this assay was close to the Michaelis–Menten constant (K_M) for each kinase. The reaction was stopped after 1 hour, and the incorporation of ³³P was quantified using a scintillation counter. Inhibition was measured by the residual activity of ³³P: Lower residual activity indicated higher inhibitor potency for the specific kinase. Based on the 335-kinase screen, 24 kinases showing >50% inhibition were selected for focused IC₅₀ determination using the same assay at 10 concentrations of NVL-520 in semilogarithmic steps (3 μ mol/L, 900 nmol/L, 300 nmol/L, 90 nmol/L, ..., 0.09 nmol/L). IC₅₀ was determined from the plot of residual activity against log (inhibitor concentration) regressed to a four-parameter logistic equation. Kinome map illustration reproduced courtesy of Cell Signaling Technology, Inc. (www.cellsignal.com; ref. 64).

Cell Culture

All cells were maintained at 37°C with 5% CO₂. Ba/F3 cells were provided by the RIKEN BRC through the National Bio-Resource Project of the MEXT, Japan. Ba/F3 cells were maintained in RPMI 1640 + 10% FBS. Genes encoding human CD74-ROS1 (with wild-type kinase domain or with S1986F, L2026M, G2032R, D2033N, or L2086F mutation), TPM3-TRKA, ETV6-TRKB, ETV6-TRKC, or TRKB (full length), or EGFR L858R/T790M/C797S were synthesized, cloned into a retroviral vector with a puromycin resistance marker, and packaged into retroviral particles. The virus was used to infect Ba/F3 cells. Stable cell lines were selected by IL3 withdrawal and with puromycin for at least 7 days. The polyclonal culture was used in assays directly, or monoclonal cultures were established through limiting dilution before being used in assays. Successful transformants were confirmed by Sanger sequencing and Western blot. All cells were confirmed to express the full desired protein. Ba/F3 CD74-ROS1 contained a small C-terminal truncation, and Ba/F3 ETV6-TRKC contained a small C-terminal frameshift. Both were confirmed by orthogonal assays to have no discernible effects on inhibitor activity. HCC78, A431, NCI-H1975, NCI-H2228, NCI-H3122, and

A549 cell lines were obtained at Pharmaron. The MGH193-1 (41) cell line was developed from a malignant pleural effusion of a treatment-naive patient with NSCLC harboring *EZR-ROS1* rearrangement and was verified by detection of the *EZR-ROS1* fusion transcript by RT-PCR (both *EZR1-ROS1* fusion junction and *ROS1* kinase domain). The MGH9018-1 (65) cell line was developed from malignant pleural effusion of a patient with crizotinib-resistant NSCLC harboring *CD74-ROS1* G2032R rearrangement and was verified by detection of the *CD74-ROS1* fusion transcript by RT-PCR (both *CD74-ROS1* fusion junction and *ROS1* kinase domain) and detection of the G2032R mutation by Sanger sequencing. Methods of cell line generation have been previously published (66). Prior to model generation, the patients provided written informed consent to participate in a Dana-Farber and Harvard Cancer Center Institutional Review Board-approved protocol giving permission for research to be performed on their samples. Cell lines were cultured in RPMI 1640 with 10% FBS and were sequenced to confirm the presence of *ROS1* rearrangement and mutation. Additional authentication was performed by SNP fingerprinting.

Alternatively, Ba/F3 cells expressing the following genes were made separately. *ROS1* fusion mutants were made using site-directed mutagenesis (Agilent, New England Biolabs). Platinum-E cells (Cell Biolabs, Inc.) were transfected with pBABE *CD74-ROS1*, pMIG *CEP85L-ROS1*, pCX4 *EZR-ROS1*, pBABE *GOPC(S)-ROS1*, pCX4 *GOPC(S)-ROS1*, pBABE *GOPC(L)-ROS1*, pCX4 *GOPC(L)-ROS1*, or pMIG *SLC34A2-ROS1* wild-type or mutant constructs using Biotool DNA transfection reagent to generate replication incompetent, ecotropic retrovirus. Ba/F3 parental cells were infected with retrovirus. Cells were treated with puromycin to select for cells stably expressing the respective fusions. Cells that survived IL3 withdrawal were used for *in vitro* assays. All transformed cell lines were sequenced to verify the presence of desired mutations. Cells were harvested and pelleted, and DNA was extracted using QuickExtract DNA Extraction Solution (Lucigen). The *ROS1* kinase and C-terminal domains were PCR amplified. Benchling software was used to align chromatographs to confirm the presence of desired mutations and verify that no undesired mutations were introduced during viral transduction.

All cells were inspected for *Mycoplasma* contamination using the ABM PCR Mycoplasma Detection Kit (cat. #G238) or the Lonza MycoAlert Detection Kit (LT07-710) at a frequency of at least once every 3 months.

Cell Viability Assay

Protocols varied slightly with the testing site. For testing site A, A549 or stable Ba/F3 cells were seeded into 384-well plates, and test compounds were added in a 3-fold dilution series in complete culture medium containing 10% FBS. After a 72-hour incubation with the inhibitor, cell viability was measured using the CellTiter-Glo reagent (Promega). Untreated wells served as negative controls (no inhibition of proliferation), whereas wells treated with high concentrations of the nonspecific kinase inhibitor staurosporine served as positive controls (full inhibition of proliferation). IC_{50} was calculated from percent inhibition and log (inhibitor concentration) using four-parameter logistic regression.

For testing site B, all inhibitors were prepared as 1 mmol/L stocks in DMSO. Plates were preseeded with 25 μ L per well of complete medium using a Multidrop Combi Reagent Dispenser (Thermo Scientific). Inhibitors were distributed onto 384-well plates at 2-fold of the indicated concentrations into 25 μ L per well of complete medium using a D300 Digital Dispenser (Hewlett-Packard). Ba/F3 cell lines expressing wild-type or mutant *ROS1* fusions were seeded at 1,000 cells per well in a volume of 25 μ L using a Multidrop Combi Reagent Dispenser (Thermo Scientific). Plates were incubated for 72 hours. Viability was measured using a WST-8 [2-(2-methoxy-4-nitrophenyl)-3-(4-nitrophenyl)-5-(2,4-disulfophenyl)-2H-tetrazolium, monosodium salt]-based assay (Bimake) and read on a Biotek Synergy 2 plate reader. Each condition was assayed in triplicate. Data were normalized using

Microsoft Excel, and IC_{50} values were calculated using a nonlinear regression analysis in GraphPad Prism.

For testing site C, MGH193-1 and MGH9018-1 cells were plated at 4,000 cells/well in triplicate into 96-well plates. Cells were incubated with CellTiter-Glo (Promega) after 5-day drug treatment, and luminescence was measured with a SpectraMax M5 Multimode Microplate Reader (Molecular Devices, LLC). GraphPad Prism (GraphPad Software) was used to graphically display data and determine IC_{50} values by a nonlinear regression model utilizing a four-parameter analytic method.

In some human cancer cell lines, we observed that NVL-520 showed biphasic dose-response behavior. We attributed the first dose response to on-target growth inhibition caused by *ROS1* inhibition and the second dose response to off-target cytotoxicity caused by pathways beyond *ROS1* inhibition. In such cases, only the first IC_{50} values are reported and indicate on-target *ROS1* inhibition.

Cellular Phosphorylation Assay

For the Ba/F3 TRKB cell phosphorylation assay, cells were seeded into 384-well plates, and test compounds were added in a 3-fold dilution series in full culture medium + 10% FBS. Cells were stimulated with 100 ng/mL BDNF for 20 minutes. TRK phosphorylation was measured using the phospho-TRKA (Tyr674/675)/phospho-TRKB (Tyr706/Tyr707) AlphaLISA reagent (PerkinElmer, #ALSU-PTRKAB). Untreated wells served as negative controls (no inhibition), whereas wells treated with high concentrations of the nonspecific kinase inhibitor staurosporine served as positive controls (full inhibition). IC_{50} was calculated from percent inhibition and inhibitor concentration using four-parameter logistic regression.

NIH3T3 cells expressing *EZR-ROS1* wild-type or mutant fusions were treated with the indicated concentrations of inhibitor for 3 hours prior to harvest. Cells were washed with phosphate-buffered saline (PBS) and harvested with cell lysis buffer supplemented with 0.25% deoxycholate, 0.05% SDS, and protease and phosphatase inhibitors. Protein concentrations were determined using the Pierce BCA Protein Assay (Thermo Fisher Scientific). Lysates were extracted using Laemmli sample buffer supplemented with beta-mercaptoethanol for 10 minutes at 75°C, and lysates were run on 4% to 20% precast gradient Bis-tris gels (Invitrogen; Thermo Fisher Scientific). Proteins were transferred to nitrocellulose membranes (Prometheus) and probed with phospho-*ROS1* Y2274 (3078; 1:1,000; Cell Signaling Technology), DYKDDDDK [Flag] (8H8L17; 1:1,000; Invitrogen), phospho-SHP2 (A5278; 1:1,000; Bimake), phospho-ERK1/2 (9101; 1:1,000; Cell Signaling Technology), ERK2 (sc-1647; 1:1,000; Santa Cruz), phospho-S6 (4858; 1:1,000; Cell Signaling Technology), S6 (2216; 1:1,000; Cell Signaling Technology), phospho-Akt (4060; 1:1,000; Cell Signaling Technology), Akt (9272; 1:1,000; Cell Signaling Technology), or Actin (JLA-20; 1:5,000; Developmental Studies Hybridoma Bank). Signal was detected using HRP-conjugated or IRDye secondary antibodies on a Bio-Rad ChemiDoc imaging station or a LI-COR Odyssey imaging station, respectively.

MGH193-1 and MGH9018-1 were treated for 6 hours. Total protein lysates were analyzed by Western blotting with the following antibodies (all from Cell Signaling Technology): phospho-*ROS1* Y2274 (3078), *ROS1* (3287), phospho-AKT S473 (4060), AKT (4691), phospho-ERK1/2 T202/Y204 (9101), ERK1/2 (9102), phospho-S6 S240/244 (5364), S6 (2217), and β -Actin (4970).

Colony Formation Assay

Plates were preseeded with 0.8% agarose in complete medium with either DMSO or inhibitor (crizotinib, entrectinib, lorlatinib, or NVL-520 at 10, 100, or 1,000 nmol/L). Each inhibitor was paired with its own DMSO condition to serve as an accurate control. NIH3T3 cells expressing *CD74-ROS1* or *EZR-ROS1* wild-type or mutant fusions were plated in 0.4% agarose in complete medium at a density of 2,000 cells per 0.5 mL of agarose with DMSO or inhibitor at an identical concentration to the bottom layer. Plates were incubated for 4 weeks,

and each well was fed 3× per week with 75 μL of complete medium with or without inhibitor to match each plated condition to prevent drying of the agarose. Plates were read after 3 and 4 weeks using Gel-Count (Oxford Optronix). Colony counts were averaged by condition and normalized to the colony counts from paired DMSO conditions. Data analysis and visualization were performed using Microsoft Excel and GraphPad Prism.

In Vivo Studies

Subcutaneous Xenograft Studies. CTG-0848 PDX. The experimental procedures were performed according to the guidelines approved by the Institutional Animal Care and Use Committee (IACUC) of Champions Oncology, accredited by the Association for Assessment and Accreditation of Laboratory Animal Care (AAALAC). Female athymic Nude-Foxn1^{nu} mice were implanted subcutaneously into the left flank with tumor fragments from the CTG-0848 model. In the efficacy study, after tumors grew to 150 to 300 mm³, mice ($n = 3-5$ /group) were randomized and administered vehicle or NVL-520 by oral gavage b.i.d. (12-hour intervals). In a separate pharmacokinetic (PK) and pharmacodynamic (PD) study, after tumors grew to 350 to 500 mm³, mice received a single dose or b.i.d. × 5 days of vehicle or NVL-520, and tumor and blood were collected at 1 hour and 12 hours (treatment only) after dose. The model was verified by vendor-provided NGS to contain a heterozygous *CD74-ROS1* fusion.

Lu01-0414 PDX. All the procedures related to animal handling, care, and treatment in study were performed according to the guidelines approved by the IACUC of WuXi AppTec following the guidance of the AAALAC. Female Balb/c nude mice were implanted subcutaneously into the right flank with tumor slices (~30 mm³) from the Lu01-0414 model. In the efficacy study, after tumors grew to an average tumor volume of 160 mm³, mice ($n = 3-5$ /group) were randomized and administered by oral gavage b.i.d. (12-hour intervals) vehicle or NVL-520. In a separate PK and PD study, after tumors grew to an average tumor volume of 492 mm³, mice received a single dose or b.i.d. × 5 days of vehicle or NVL-520, and tumor and blood were collected at 1 hour and 12 hours (treatment only) after dose. The model was verified by vendor-provided NGS to contain a heterozygous *SDC4-ROS1* fusion with a linkage between the SDC4 L66 residue and the ROS1 A1750 residue.

MGH9018-1 PDX. The study was conducted in accordance with the guidelines as published in the Guide for the Care and Use of Laboratory Animals and was approved by the IACUC of Massachusetts General Hospital. Xenografts were implanted subcutaneously into the flanks of female athymic nude (Nu/Nu) mice ages 6 to 8 weeks. Mice were maintained in laminar flow units in sterile filter-top cages with Alpha-Dri bedding. Mice were randomized into groups once the tumors had attained a volume of 150 mm³. The treatment groups were treated with drug solution dissolved in acid water once a day (crizotinib) or drug solution dissolved in 20% hydroxypropyl-β-cyclodextrin (HP-β-CD) twice a day at 9/15-hour intervals (NVL-520) by oral gavage. Tumor volumes were measured twice weekly and calculated using the formula: $\text{mm}^3 = 0.52 \times L \times W^2$. For protein assays, tumor-bearing mice were administered drugs for 3 days according to the above dosing schedule, and tumors were harvested 3 hours after the last treatment for Western blotting.

CTG-2532 PDX. The experimental procedures were performed according to the guidelines approved by the IACUC of Champions Oncology, accredited by AAALAC. Female athymic Nude-Foxn1^{nu} mice were implanted subcutaneously into the left flank with tumor fragments from model CTG-2532. In the efficacy study, after tumors grew to 150 to 300 mm³, mice ($n = 5$ /group) were administered vehicle, NVL-520, or repotrectinib by oral gavage b.i.d. (12-hour intervals) for up to 21 days (b.i.d. × 21 days) if tolerated. Repotrectinib (DC Chemicals) was dosed as a suspension solution containing 0.5%

carboxymethylcellulose and 1% Tween-80. The dosing suspension was stored 2–8°C in the dark for up to 7 days with continuous stirring. In a separate PK and PD study, CTG-2532 tumors were subcutaneously implanted in mice and allowed to grow to 350 to 550 mm³ before a single dose of the vehicle or NVL-520 was administered. Tumor and blood were collected at 1 hour and 12 hours (treatment only) after dose for PK and PD analysis. The model was verified by vendor-provided NGS to harbor a *CD74-ROS1* G2032R.

Ba/F3 CD74-ROS1 G2032R CDX. All the procedures related to animal handling, care, and treatment in this study were performed according to guidelines approved by the IACUC of Pharmaron following the guidance of the AAALAC. Six- to 8-week-old female Balb/c nude mice were inoculated subcutaneously on the right flank with 1×10^6 Ba/F3 CD74-ROS1 G2032R cells. After the tumors reached a mean tumor volume of approximately 128 mm³, treatment was initiated, and tumors and body weight were measured at regular intervals.

Plasma drug concentrations were determined by LC/MS. Free drug concentrations were calculated by multiplying the total concentration values determined from PK experiments with the corresponding fraction unbound in mouse plasma (= 7.7% for NVL-520 and = 7.6% for crizotinib; Pharmaron).

K_{p,uu} and Intracranial Studies

All the procedures related to animal handling, care, and treatment in these studies were performed according to guidelines approved by the IACUC of Pharmaron following the guidance of AAALAC.

NVL-520 was formulated as 1 mg/mL suspension in 20% HP-β-CD in deionized water. Lorlatinib was formulated as a 1 mg/mL solution in two equivalents of HCl + 20% HP-β-CD in deionized water. Compounds were administered orally to male Wistar Han rats ($n = 3$ each). After 1 hour, brain samples and plasma were collected, and brain samples were homogenized in PBS. Brain and plasma samples were precipitated by acetonitrile and centrifugation (4,700 rpm, 15 minutes). Drug concentrations in the supernatants were quantified by LC/MS-MS. Unbound fractions were determined using rapid equilibrium dialysis. K_{p,uu} was calculated as the ratio between unbound drug concentration in the brain and unbound drug concentration in the plasma.

Ba/F3 CD74-ROS1 G2032R cells were transduced with viral particles containing the firefly luciferase gene and a neomycin resistance marker. Infected cells were selected on neomycin, and monoclonal cultures were established through limiting dilution. Successful transformants were confirmed by Sanger sequencing and bioluminescence. For the *in vivo* study, 1×10^5 Ba/F3 CD74-ROS1 G2032R luciferase cells were stereotactically implanted into the right forebrains of 6- to 8-week-old female Balb/c nude mice. After 5 days, mice were randomized based on mean bioluminescence signal into three groups of $n = 7-10$ mice each and received vehicle or NVL-520, 2 mg/kg, orally, b.i.d. Bioluminescence and body weight were measured at regular intervals until the end of the study (61 days after treatment start) or until animals met the criteria for euthanasia.

Clinical Study

ARROS-1 (NCT05118789) is a first-in-human, tumor-agnostic phase I/II trial of NVL-520 in patients with solid tumors harboring ROS1 rearrangements (45). All patients provided written informed consent for participation. The study was conducted in accordance with the ethical principles of Good Clinical Practice and the Declaration of Helsinki and was approved by the institutional review board/independent ethics committee at each participating site. Case studies are reported as of the data cutoff date of September 13, 2022. The ctDNA NGS assay was conducted with plasma from whole blood collected at pre-dose on C1D1 and C1D15 using the Guardant360 assay (Guardant Health). Patient blood samples for PK analysis were collected at predose and then 0.25,

0.5, 1, 2, 4, 6, and 24 hours after dose. Blood samples were processed to plasma and analyzed using a validated LC/MS-MS method.

Data Availability

No datasets were generated or analyzed in this study.

Authors' Disclosures

A. Drilon reports personal fees from Nuvalent, Inc. during the conduct of the study; personal fees from Ignyta, Genentech, Roche, MORE Health, AXIS, Loxo, Eli Lilly, Bayer, AbbVie, EPG Health, Takeda, Ariad, Millenium, 14ner, Elevation Oncology, Harborside Nexus, TP Therapeutics, ArcherDX, Liberum, AstraZeneca, Monopteros, RV More, Pfizer, Novartis, Ology, Blueprint Medicines, EMD Serono, Amgen, Helsinn, Medendi, TouchIME, BeiGene, Repare RX, Janssen, BergenBio, Entos, Hengrui Therapeutics, Merus, Treeline Bio, Exelixis, Chugai Pharmaceutical, Prelude, Tyra Biosciences, Remedica Ltd., Applied Pharmaceutical Science, Inc., Verastem, mBrace, Treeline, MonteRosa, AXIS, AiCME, I3 Health, Innocare, and Boundless Bio outside the submitted work; a patent for osimertinib-selpercatinib pending; prior research funding from Foundation Medicine; associated research paid to institution from Pfizer, Exelixis, GSK, Teva, Taiho, and PharmaMar; royalties from Wolters Kluwer; other (food/beverage) from Merck, Puma, Merus, and Boehringer Ingelheim; and CME honoraria from Medscape, OncLive, PeerVoice, Physicians' Education Resources, Targeted Oncology, Research to Practice, Axis, Peerview Institute, Paradigm Medical Communications, WebMD, MJH Life Sciences, AXIS, EPG Health, JNCC/Harborside, I3 Health, Liberum, Remedica Ltd., and Lungevity. J.C. Horan reports employment with and ownership interest in Nuvalent, Inc., and a patent for WO 2021/226208 pending and a patent for PCT/US2022/077323 pending. A. Tangpeerachaikul reports employment with and ownership interest in Nuvalent, Inc., and a patent for WO 2021/226208 pending and a patent for CT/US2022/077364 pending. B. Besse reports grants from 4D Pharma, AbbVie, Amgen, Aptitude Health, AstraZeneca, BeiGene, Blueprint Medicines, Boehringer Ingelheim, Celgene, Cergentis, Chugai Pharmaceutical, Cristal Therapeutics, Daiichi Sankyo, Eli Lilly, Eisai, Genzyme Corporation, GSK, Inivata, Ipsen, Janssen, Onxeo, OSE Immunotherapeutics, Pfizer, Roche/Genentech, Sanofi, Takeda, Tolero Pharmaceuticals, Turning Point Therapeutics, and Nuvalent, Inc. during the conduct of the study. S.-H.I. Ou reports grants from Nuvalent, Inc. during the conduct of the study, as well as personal fees from Pfizer, Johnson & Johnson/Janssen, Eli Lilly, BeiGene, and Merus, personal fees and nonfinancial support from Elevation Oncology, and nonfinancial support from Turning Point Therapeutics, BlossomHill Therapeutics, and MBrace Therapeutics outside the submitted work. S.M. Gadgeel reports grants from Nuvalent, Inc. during the conduct of the study, as well as consultancy for AstraZeneca, Pfizer, Takeda, Merck, Blueprint, Mirati, Genentech/Roche, Merck, Esai, Eli Lilly, and GSK, travel support to ESMO from Mirati, and independent data monitoring committee member for AstraZeneca. D.R. Camidge reports personal fees from Nuvalent, Inc. during the conduct of the study, as well as personal fees from Anheart, Pfizer, Turning Point, and Roche outside the submitted work. A.J. van der Wekken reports grants and other support from AstraZeneca, Boehringer Ingelheim, Pfizer, Roche, and Takeda, and other support from Janssen and Eli Lilly outside the submitted work. C. Keddy reports grants and nonfinancial support from Nuvalent, Inc. during the conduct of the study. K.S. Nicholson reports grants and nonfinancial support from Nuvalent, Inc. during the conduct of the study. S. Yoda reports grants from Nuvalent, Inc. during the conduct of the study, as well as grants and personal fees from Nuvalent Inc., and personal fees from Pfizer Japan and Tango Therapeutics outside the submitted work. S. Mente reports employment with and ownership interest in Nuvalent, Inc., and a patent for WO 2021/226208 pending. Y.

Sun reports employment with and ownership interest in Nuvalent, Inc. J.R. Soglia reports employment with and ownership interest in Nuvalent, Inc., and a patent for PCT/US2022/077364 pending. N.E. Kohl reports personal fees from Nuvalent, Inc. during the conduct of the study. J.R. Porter is a board member and employee of and has ownership interest in Nuvalent, Inc., and reports a patent for PCT/US2022/077364 pending. M.D. Shair is a consultant/board member of and has ownership interest in Nuvalent, Inc. during the conduct of the study; has employment with Harvard University outside the submitted work; and reports a patent for WO 2021/226208 pending. V. Zhu reports employment with and ownership interest in Nuvalent, Inc. during the conduct of the study, as well as other support from AstraZeneca, BeiGene, Blueprint, Roche/Foundation Medicine, Roche/Genentech, Takeda, Xcovery, and TP Therapeutics outside the submitted work. M.A. Davare reports grants from Nuvalent, Inc. during the conduct of the study. A.N. Hata reports grants and personal fees from Nuvalent, Inc. during the conduct of the study, as well as grants from Pfizer, Amgen, Eli Lilly, Roche/Genentech, Blueprint Medicines, C4 Therapeutics, BridgeBio, Novartis, Bristol Myers Squibb, and Scorpion Therapeutics and personal fees from Tigenix, Engine Biosciences, and Tolremo Therapeutics outside the submitted work. H.E. Plish reports employment with and ownership interest in Nuvalent, Inc., and a patent for WO 2021/226208 pending and a patent for PCT/US2022/077364 pending. J.J. Lin reports personal fees and other support from Nuvalent, Inc. during the conduct of the study, as well as personal fees and other support from Roche/Genentech, Bayer, Elevation Oncology, Novartis, Pfizer, and Turning Point Therapeutics, personal fees from Regeneron, Blueprint Medicines, and Mirati Therapeutics, and other support from Hengrui Therapeutics, Neon Therapeutics, Relay Therapeutics, and Linnaeus Therapeutics outside of the submitted work. No disclosures were reported by the other authors.

Authors' Contributions

A. Drilon: Resources, supervision, investigation, writing—original draft, writing—review and editing. **J.C. Horan:** Conceptualization, data curation, software, formal analysis, investigation, project administration, writing—review and editing. **A. Tangpeerachaikul:** Conceptualization, formal analysis, supervision, investigation, visualization, methodology, writing—original draft, writing—review and editing. **B. Besse:** Data curation, investigation, writing—review and editing. **S.-H.I. Ou:** Resources, data curation, investigation, writing—review and editing. **S.M. Gadgeel:** Data curation, investigation, writing—review and editing. **D.R. Camidge:** Data curation, investigation, writing—review and editing. **A.J. van der Wekken:** Data curation, investigation, writing—review and editing. **L. Nguyen-Phuong:** Investigation. **A. Acker:** Investigation. **C. Keddy:** Formal analysis, validation, investigation, methodology. **K.S. Nicholson:** Formal analysis, validation, investigation, methodology. **S. Yoda:** Conceptualization, formal analysis, validation, investigation. **S. Mente:** Formal analysis, visualization, methodology, writing—review and editing. **Y. Sun:** Investigation, visualization. **J.R. Soglia:** Validation, investigation. **N.E. Kohl:** Conceptualization, supervision, methodology, writing—review and editing. **J.R. Porter:** Conceptualization, supervision, funding acquisition, project administration, writing—review and editing. **M.D. Shair:** Conceptualization, supervision, funding acquisition, writing—review and editing. **V. Zhu:** Conceptualization, data curation, formal analysis, validation, investigation, writing—review and editing. **M.A. Davare:** Conceptualization, resources, formal analysis, supervision, validation, writing—review and editing. **A.N. Hata:** Conceptualization, resources, supervision, funding acquisition, validation, writing—review and editing. **H.E. Plish:** Conceptualization, supervision, funding acquisition, investigation, methodology, project administration, writing—review and editing. **J.J. Lin:** Conceptualization, resources, supervision, investigation, visualization, writing—original draft, writing—review and editing.

Acknowledgments

We thank the patients, caregivers, advocates, physicians, nurses, and research staff for their participation in the ongoing ARROS-1 clinical trial. This work was funded by Nuvalent, Inc. A. Drilon was supported in part by the P30 CA008748 grant from the NCI of the NIH. J.J. Lin was supported in part by NIH/NCI R01CA164273.

The publication costs of this article were defrayed in part by the payment of publication fees. Therefore, and solely to indicate this fact, this article is hereby marked “advertisement” in accordance with 18 USC section 1734.

Note

Supplementary data for this article are available at Cancer Discovery Online (<http://cancerdiscovery.aacrjournals.org/>).

Received August 30, 2022; revised October 10, 2022; accepted November 28, 2022; published first December 13, 2022.

REFERENCES

- Drilon A, Jenkins C, Iyer S, Schoenfeld A, Keddy C, Davare MA. ROS1-dependent cancers – biology, diagnostics and therapeutics. *Nat Rev Clin Oncol* 2021;18:35–55.
- Lin JJ, Shaw AT. Recent advances in targeting ROS1 in lung cancer. *J Thorac Oncol* 2017;12:1611–25.
- Gu TL, Deng X, Huang F, Tucker M, Crosby K, Rimkunas V, et al. Survey of tyrosine kinase signaling reveals ROS kinase fusions in human cholangiocarcinoma. *PLoS One* 2011;6:e15640.
- Charest A, Lane K, McMahon K, Park J, Preisinger E, Conroy H, et al. Fusion of FIG to the receptor tyrosine kinase ROS in a glioblastoma with an interstitial del(6)(q21q21). *Genes Chromosomes Cancer* 2003;37:58–71.
- Marks EI, Pamarthy S, Dizon D, Birnbaum A, Yakirevich E, Safran H, et al. ROS1-GOPC/FIG: a novel gene fusion in hepatic angiosarcoma. *Oncotarget* 2019;10:245–51.
- Birch AH, Arcand SL, Oros KK, Rahimi K, Watters AK, Provencher D, et al. Chromosome 3 anomalies investigated by genome wide SNP analysis of benign, low malignant potential and low grade ovarian serous tumours. *PLoS One* 2011;6:e28250.
- Ou SHI, Nagasaka M. A catalog of 5' fusion partners in ROS1-positive NSCLC circa 2020. *JTO Clin Res Rep* 2020;1:100048.
- Li Z, Shen L, Ding D, Huang J, Zhang J, Chen Z, et al. Efficacy of crizotinib among different types of ROS1 fusion partners in patients with ROS1-rearranged non-small cell lung cancer. *J Thorac Oncol* 2018;13:987–95.
- Neel DS, Allegakoen DV, Olivas V, Mayekar MK, Hemmati G, Chatterjee N, et al. Differential subcellular localization regulates oncogenic signaling by ROS1 kinase fusion proteins. *Cancer Res* 2019;79:546–56.
- Keddy C, Shinde P, Jones K, Kaech S, Somwar R, Shinde U, et al. Resistance profile and structural modeling of next-generation ROS1 tyrosine kinase inhibitors. *Mol Cancer Ther* 2022;21:336–46.
- Shaw AT, Riely GJ, Bang YJ, Kim DW, Camidge DR, Solomon BJ, et al. Crizotinib in ROS1-rearranged advanced non-small-cell lung cancer (NSCLC): updated results, including overall survival, from PROFILE 1001. *Ann Oncol* 2019;30:1121–6.
- Drilon A, Siena S, Dziadziuszko R, Barlesi F, Krebs MG, Shaw AT, et al. Entrectinib in ROS1 fusion-positive non-small-cell lung cancer: integrated analysis of three phase 1–2 trials. *Lancet Oncol* 2020;21:261–70.
- Shaw AT, Solomon BJ, Chiari R, Riely GJ, Besse B, Soo RA, et al. Lorlatinib in advanced ROS1-positive non-small-cell lung cancer: a multicentre, open-label, single-arm, phase 1–2 trial. *Lancet Oncol* 2019;20:1691–701.
- National Comprehensive Cancer Network. NCCN clinical practice guidelines in oncology (NCCN Guidelines®) non-small cell lung cancer [cited 2022 Nov 16]. Available from: <https://www.nccn.org>.
- Ou SHI, Fujiwara Y, Shaw AT, Yamamoto N, Nakagawa K, Fan F, et al. Efficacy of taletrectinib (AB-106/DS-6051b) in ROS1+ NSCLC: An updated pooled analysis of U.S. and Japan phase 1 studies. *JTO Clin Res Rep* 2021;2:100108.
- Drilon A, Cho BC, Kim DW, Lee J, Lin JJ, Zhu V, et al. Safety and preliminary clinical activity of repotrectinib in patients with advanced ROS1/TRK fusion-positive solid tumors (TRIDENT-1 study). *Ann Oncol* 2019;30 Suppl 5:v162. Abstract nr 444PD.
- Aldea M, Besse B, Hendriks LEL. ALK inhibitors in ALK-positive NSCLC with central nervous system metastases. *Eur Oncol Haematol* 2020;16:18–21.
- Ou SHI, Zhu VW. CNS metastasis in ROS1+ NSCLC: An urgent call to action, to understand, and to overcome. *Lung Cancer* 2019;130:201–7.
- Patil T, Smith DE, Bunn PA, Aisner DL, Le AT, Hancock M, et al. The incidence of brain metastases in stage IV ROS1-rearranged non-small cell lung cancer and rate of central nervous system progression on crizotinib. *J Thorac Oncol* 2018;13:1717–26.
- Lin JJ, Choudhury NJ, Yoda S, Zhu VW, Johnson TW, Sakhtemani R, et al. Spectrum of mechanisms of resistance to crizotinib and lorlatinib in ROS1 fusion-positive lung cancer. *Clin Cancer Res* 2021;27:2899–909.
- Doebele R, Dziadziuszko R, Drilon A, Shaw A, Wolf J, Farago A, et al. Genomic landscape of entrectinib resistance from ctDNA analysis in STARTRK-2. *Ann Oncol* 2019;30 Suppl 5:v865. Abstract nr LBA28.
- Facchinetti F, Loriot Y, Kuo M-S, Mahjoubi L, Lacroix L, Planchard D, et al. Crizotinib-resistant ROS1 mutations reveal a predictive kinase inhibitor sensitivity model for ROS1- and ALK-rearranged lung cancers. *Clin Cancer Res* 2016;22:5983–91.
- Ko HJ, Hsu CK, Yeh YC, Huang HC. ROS-1 TKI for the treatment of concurrent sarcomatoid transformation and acquired ROS-1 F2004C mutation in a lung adenocarcinoma patient. *Pulmonology* 2022;28:76–9.
- Dimou A, Ou SHI, Doebele RC. Dramatic response to lorlatinib in a patient with CD74-ROS1-positive lung adenocarcinoma with acquired F2004V mutation. *JCO Precis Oncol* 2019;3:PO.19.00013.
- McCoach CE, Le AT, Gowan K, Jones K, Schubert L, Doak A, et al. Resistance mechanisms to targeted therapies in ROS1(+) and ALK(+) non-small cell lung cancer. *Clin Cancer Res* 2018;24:3334–47.
- Drilon A, Somwar R, Wagner JP, Vellore NA, Eide CA, Zabriskie MS, et al. A novel crizotinib-resistant solvent-front mutation responsive to cabozantinib therapy in a patient with ROS1-rearranged lung cancer. *Clin Cancer Res* 2016;22:2351–8.
- Begum P, Cui W, Papat S. Crizotinib-resistant ROS1 G2101A mutation associated with sensitivity to lorlatinib in ROS1-rearranged non-small cell lung cancer: Case Report. *JTO Clin Res Rep* 2022;3:100376.
- Li W, Yang N, Ma H, Fan H, Li K, Wu H, et al. The efficacy and safety of taletrectinib in patients with TKI-naïve or crizotinib-pretreated ROS1-positive non-small cell lung cancer (NSCLC). *J Clin Oncol* 40, 2022 (suppl 16; abstr 8572).
- Cho BC, Lin J, Camidge DR, Velcheti V, Solomon B, Lu S, et al. Pivotal topline data from the phase 1/2 TRIDENT-1 trial of repotrectinib in patients with ROS1+ advanced non-small cell lung cancer (NSCLC). *Eur J Cancer* 2022;174:S1–2.
- Cocco E, Scaltriti M, Drilon A. NTRK fusion-positive cancers and TRK inhibitor therapy. *Nat Rev Clin Oncol* 2018;15:731–47.
- Shaw AT, Bauer TM, de Marinis F, Felip E, Goto Y, Liu G, et al. First-line lorlatinib or crizotinib in advanced ALK-positive lung cancer. *N Engl J Med* 2020;383:2018–29.
- Drilon A, Ou SHI, Cho BC, Kim DW, Lee J, Lin JJ, et al. Repotrectinib (TPX-0005) is a next-generation ROS1/TRK/ALK inhibitor that potently inhibits ROS1/TRK/ALK solvent-front mutations. *Cancer Discov* 2018;8:1227–36.
- Liu D, Flory J, Lin A, Offin M, Falcon CJ, Murciano-Goroff YR, et al. Characterization of on-target adverse events caused by TRK inhibitor therapy. *Ann Oncol* 2020;31:1207–15.
- Zou HY, Li Q, Engstrom LD, West M, Appleman V, Wong KA, et al. PF-06463922 is a potent and selective next-generation ROS1/ALK inhibitor capable of blocking crizotinib-resistant ROS1 mutations. *Proc Natl Acad Sci U S A* 2015;112:3493–8.

35. Awad MM, Katayama R, McTigue M, Liu W, Deng YL, Brooun A, et al. Acquired resistance to crizotinib from a mutation in CD74-ROS1. *N Engl J Med* 2013;368:2395–401.
36. Wang L, Wu Y, Deng Y, Kim B, Pierce L, Krilov G, et al. Accurate and reliable prediction of relative ligand binding potency in prospective drug discovery by way of a modern free-energy calculation protocol and force field. *J Am Chem Soc* 2015;137:2695–703.
37. Abel R, Wang L, Harder ED, Berne BJ, Friesner RA. Advancing drug discovery through enhanced free energy calculations. *Acc Chem Res* 2017;50:1625–32.
38. Wager TT, Hou X, Verhoest PR, Villalobos A. Central nervous system multiparameter optimization desirability: application in drug discovery. *ACS Chem Neurosci* 2016;7:767–75.
39. Paoli P, Giannoni E, Chiarugi P. Anoinis molecular pathways and its role in cancer progression. *Biochim Biophys Acta* 2013;1833:3481–98.
40. Hanahan D, Weinberg RA. The hallmarks of cancer. *Cell* 2000;100:57–70.
41. Katayama R, Gong B, Togashi N, Miyamoto M, Kiga M, Iwasaki S, et al. The new-generation selective ROS1/NTRK inhibitor DS-6051b overcomes crizotinib resistant ROS1-G2032R mutation in preclinical models. *Nat Commun* 2019;10:3604.
42. Bauer TM, Shaw AT, Johnson ML, Navarro A, Gainor JF, Thurm H, et al. Brain penetration of lorlatinib: cumulative incidences of CNS and non-CNS progression with lorlatinib in patients with previously treated ALK-positive non-small-cell lung cancer. *Target Oncol* 2020;15:55–65.
43. Johnson TW, Richardson PF, Bailey S, Brooun A, Burke BJ, Collins MR, et al. Discovery of (10 R)-7-Amino-12-fluoro-2,10,16-trimethyl-15-oxo-10,15,16,17-tetrahydro-2H-8,4-(metheno)pyrazolo[4,3-h][2,5,11]-benzoxadiazacyclotetradecine-3-carbonitrile (PF-06463922), a macrocyclic inhibitor of anaplastic lymphoma kinase (ALK) and c-ros oncogene 1 (ROS1) with preclinical brain exposure and broad-spectrum potency against ALK-resistant mutations. *J Med Chem* 2014;57:4720–44.
44. Shaw AT, Felip E, Bauer TM, Besse B, Navarro A, Postel-Vinay S, et al. Lorlatinib in non-small-cell lung cancer with ALK or ROS1 rearrangement: an international, multicentre, open-label, single-arm first-in-man phase 1 trial. *Lancet Oncol* 2017;18:1590–9.
45. Drilon A, Besse B, Camidge DR, Ou SHI, Gadgeel SM, Johnson ML, et al. Safety and preliminary clinical activity of NVL-520, a highly selective ROS1 inhibitor, in patients with advanced ROS1 fusion-positive solid tumors. *Eur J Cancer* 2022;174:S6–7.
46. Soria JC, Ohe Y, Vansteenkiste J, Reungwetwattana T, Chewaskulyong B, Lee KH, et al. Osimertinib in untreated EGFR-mutated advanced non-small-cell lung cancer. *N Engl J Med* 2018;378:113–25.
47. Peters S, Camidge DR, Shaw AT, Gadgeel S, Ahn JS, Kim D-W, et al. Alectinib versus crizotinib in untreated ALK-positive non-small-cell lung cancer. *N Engl J Med* 2017;377:829–38.
48. Shiba-Ishii A, Johnson TW, Dagogo-Jack I, Mino-Kenudson M, Johnson TR, Wei P, et al. Analysis of lorlatinib analogs reveals a roadmap for targeting diverse compound resistance mutations in ALK-positive lung cancer. *Nat Cancer* 2022;3:710–22.
49. Lin JJ, Cho BC, Springfield C, Camidge DR, Solomon B, Baik C, et al. Update from the phase 2 registrational trial of repotrectinib in TKI-pretreated patients with ROS1+ advanced non-small cell lung cancer and with NTRK+ advanced solid tumors (TRIDENT-1) [abstract]. In: Proceedings of the AACR-NCI-EORTC Virtual International Conference on Molecular Targets and Cancer Therapeutics; 2021 Oct 7–10. Philadelphia (PA): AACR; *Mol Cancer Ther* 2021;20(12 Suppl):Abstract nr P224.
50. Drilon A. TRK inhibitors in TRK fusion-positive cancers. *Ann Oncol* 2019;30:viii23–30.
51. Drilon A, Siena S, Ou SHI, Patel M, Ahn MJ, Lee J, et al. Safety and antitumor activity of the multitargeted pan-TRK, ROS1, and ALK inhibitor entrectinib: combined results from two phase I trials (ALKA-372-001 and STARTRK-1). *Cancer Discov* 2017;7:400–9.
52. Papadopoulos KP, Borazanci E, Shaw AT, Katayama R, Shimizu Y, Zhu VW, et al. U.S. phase I first-in-human study of taletrectinib (DS-6051b/AB-106), a ROS1/TRK inhibitor, in patients with advanced solid tumors. *Clin Cancer Res* 2020;26:4785–94.
53. Rikova K, Guo A, Zeng Q, Possemato A, Yu J, Haack H, et al. Global survey of phosphotyrosine signaling identifies oncogenic kinases in lung cancer. *Cell* 2007;131:1190–203.
54. Menichincheri M, Ardini E, Magnaghi P, Avanzi N, Banfi P, Bossi R, et al. Discovery of entrectinib: a new 3-aminindazole as a potent anaplastic lymphoma kinase (ALK), c-ros oncogene 1 kinase (ROS1), and pan-tropomyosin receptor kinases (Pan-TRKs) inhibitor. *J Med Chem* 2016;59:3392–408.
55. Murray BW, Rogers E, Zhai D, Deng W, Chen X, Sprengeler PA, et al. Molecular characteristics of repotrectinib that enable potent inhibition of TRK fusion proteins and resistant mutations. *Mol Cancer Ther* 2021;20:2446–56.
56. Lu C, Wu C, Ghoreishi D, Chen W, Wang L, Damm W, et al. OPLS4: Improving force field accuracy on challenging regimes of chemical space. *J Chem Theory Comput* 2021;17:4291–300.
57. Kuhn B, Tichý M, Wang L, Robinson S, Martin RE, Kuglstatler A, et al. Prospective evaluation of free energy calculations for the prioritization of cathepsin L inhibitors. *J Med Chem* 2017;60:2485–97.
58. Yu HS, Deng Y, Wu Y, Sindhikara D, Rask AR, Kimura T, et al. Accurate and reliable prediction of the binding affinities of macrocycles to their protein targets. *J Chem Theory Comput* 2017;13:6290–300.
59. Wang L, Deng Y, Wu Y, Kim B, LeBard DN, Wandschneider D, et al. Accurate modeling of scaffold hopping transformations in drug discovery. *J Chem Theory Comput* 2017;13:42–54.
60. Moraca F, Negri A, de Oliveira C, Abel R. Application of free energy perturbation (FEP+) to understanding ligand selectivity: a case study to assess selectivity between pairs of phosphodiesterases (PDE's). *J Chem Inf Model* 2019;59:2729–40.
61. Hauser K, Negron C, Albanese SK, Ray S, Steinbrecher T, Abel R, et al. Predicting resistance of clinical Abl mutations to targeted kinase inhibitors using alchemical free-energy calculations. *Commun Biol* 2018;1:70.
62. Bertrand T, Kothe M, Liu J, Dupuy A, Rak A, Berne PF, et al. The crystal structures of TrkA and TrkB suggest key regions for achieving selective inhibition. *J Mol Biol* 2012;423:439–53.
63. Shults MD, Imperiali B. Versatile fluorescence probes of protein kinase activity. *J Am Chem Soc* 2003;125:14248–9.
64. Eid S, Turk S, Volkamer A, Rippmann F, Fulle S. KinMap: a web-based tool for interactive navigation through human kinome data. *BMC Bioinf* 2017;18:16.
65. Lin JJ, Langenbacher A, Gupta P, Yoda S, Fetter IJ, Rooney M, et al. Small cell transformation of ROS1 fusion-positive lung cancer resistant to ROS1 inhibition. *NPJ Precis Oncol* 2020;4:21.
66. Crystal AS, Shaw AT, Sequist LV, Friboulet L, Niederst MJ, Lockerman EL, et al. Patient-derived models of acquired resistance can identify effective drug combinations for cancer. *Science* 2014;346:1480–6.